



저작자표시-비영리-변경금지 2.0 대한민국

이용자는 아래의 조건을 따르는 경우에 한하여 자유롭게

- 이 저작물을 복제, 배포, 전송, 전시, 공연 및 방송할 수 있습니다.

다음과 같은 조건을 따라야 합니다:



저작자표시. 귀하는 원저작자를 표시하여야 합니다.



비영리. 귀하는 이 저작물을 영리 목적으로 이용할 수 없습니다.



변경금지. 귀하는 이 저작물을 개작, 변형 또는 가공할 수 없습니다.

- 귀하는, 이 저작물의 재이용이나 배포의 경우, 이 저작물에 적용된 이용허락조건을 명확하게 나타내어야 합니다.
- 저작권자로부터 별도의 허가를 받으면 이러한 조건들은 적용되지 않습니다.

저작권법에 따른 이용자의 권리는 위의 내용에 의하여 영향을 받지 않습니다.

이것은 [이용허락규약\(Legal Code\)](#)을 이해하기 쉽게 요약한 것입니다.

[Disclaimer](#)

공학박사학위논문

**A study on the preparation of anti-reflection films
having silica nanoparticles**

실리카 나노입자를 이용한 반사방지 필름의 제조에
관한 연구

2017년 2월

서울대학교 대학원

재료공학부

임 거 산

**A study on the preparation of anti-reflection films
having silica nanoparticles**

실리카 나노입자를 이용한 반사방지 필름의 제조에
관한 연구

지도교수 장 지 영

이 논문을 공학박사 학위논문으로 제출함

2016년 10월

서울대학교 대학원

재료공학부

임 거 산

임거산의 공학박사 학위논문을 인준함

2017년 2월

위 원 장 박 종 래 (인)

부위원장 장 지 영 (인)

위 원 남 기 태 (인)

위 원 선 정 윤 (인)

위 원 박 일 성 (인)

Abstract

A study on the preparation of anti-reflection films having silica nanoparticles

Geo San Lim

Department of Materials Science and Engineering

Seoul National University

Anti-reflection optical technology alleviates reflection from material surfaces by the destructive interference of reflected light rays. Silica nanoparticles with pores have received significant attention owing to their low refractive index, which is essential for achieving an effective anti-reflection coating. A low refractive index is achieved owing to the nanoparticles' silica pores as well as macroscopic porous packing structures that are formed in the space between the nanoparticles. To enhance the performance of anti-reflection films under a wide range of conditions, their additional characteristics, such as light sensing and anti-fogging based on superhydrophilicity, were investigated.

In this study, anti-reflection films having silica nanoparticles were prepared and their characteristics and possible applications were investigated.

First, a photosensitive, double-layered anti-reflection film was prepared from a UV cured acrylate film containing a photoluminescent europium(III) complex as a high refractive index layer and a colloidal nano-silica film as a low refractive index layer. The refractive index of the high refractive index layer was tuned from 1.53 to 1.69 by increasing the composition of the europium(III) complex. The reflectance of the anti-reflection film on a glass substrate was as low as 0.48% when the refractive indices and thicknesses of the two layers were controlled. The anti-reflection film was applied as the top layer of a liquid crystal display (LCD). Since the absorption and excitation spectra of the europium(III) complex barely overlapped with the backlight spectrum of the LCD, the europium(III) complex in the anti-reflection film did not affect the displayed images. The images were visible even when the screen was illuminated by an indoor fluorescent lamp. It was also possible to highlight a specific point on the display screen using laser light. When a 405-nm-wavelength laser pointer was aimed at a specific area, the area appeared as a bright red spot.

Second, the anti-reflection coating on the polymer substrate was prepared using surface-aggregated hollow silica nanoparticles. Hollow silica

nanoparticles, 80-nm diameter and with 10-nm-thick walls, exhibited the refractive index of 1.27. By solvent swelling of the polymer substrate and penetration of UV curable acrylates into the polymer substrate, low refractive index hollow silica nanoparticles were concentrated on the coating surface, resulted in the anti-reflection layer with the refractive index of 1.34. The reflectance of about 1.0% was achieved when 20 wt% to 60 wt% of silica nanoparticles were coated on the polymer substrate. In addition, a several micrometers thick coating on the TAC substrate exhibited anti-reflective hard coating properties, showing pencil hardness of H. The anti-reflective hard coating film had the low surface reflectance of 2%, which resulted from the gradient aggregation of hollow silica nanoparticles along the thickness dimension.

Finally, superhydrophilic anti-reflection films with a single-layer structure of 150-nm-size mesoporous silica nanoparticles were prepared. Surface morphology was tuned simply by varying the mixing ratio of mesoporous silica to the binder. The fabricated films exhibited anti-reflective and anti-fogging characteristics, owing to the hydrophilicity of silica and surface roughness of the mesoporous silica layer. When a dispersion of 67 wt% of mesoporous silica was coated, the film exhibited the lowest reflectance of 0.71%. Owing to superhydrophilicity, a glass coated with 67 wt% of mesoporous silica exhibited

a good transmission clarity even after fogging.

Keywords: anti-reflection, photoluminescent, mesoporous, silica, low refractive index, superhydrophilic, anti-fogging, surface aggregation

Student Number: 2009-30155

Contents

Abstract.....	i
Contents.....	v
List of tables.....	viii
List of equations.....	ix
List of figures.....	x
Chapter I. Introduction.....	1
I-1. Anti-reflection.....	2
I-1-1. Principle of anti-reflection coating.....	2
I-1-2. Fabrication of anti-reflection coating.....	7
I-2. Photoluminescent lanthanide(III) ions.....	12
I-2-1. The photoluminescence mechanism of lanthanide(III) ions....	12
I-2-2. Applications of photoluminescent lanthanide(III) ions.....	16
I-3. Porous silica nanoparticles.....	20
I-3-1. Synthetic method of obtaining mesoporous silica nanoparticles.....	20
I-3-2. Synthesis of hollow silica nanoparticles.....	23
I-4. Superhydrophilicity.....	26
I-4-1. Definition and mechanism of superhydrophilicity.....	26

I-4-2. Applications of superhydrophilicity.....	33
I-5. References.....	35
Chapter II. Photosensitive double-layered anti-reflection film containing a europium(III) complex.....	44
II-1. Introduction.....	45
II-2. Experimental.....	47
II-3. Results and discussion.....	50
II-4. Conclusions.....	64
II-5. References.....	65
Chapter III. Anti-reflective film prepared by surface aggregation of hollow silica nanoparticles.....	67
III-1. Introduction.....	68
III-2. Experimental.....	70
III-3. Results and discussion.....	72
III-4. Conclusions.....	89
III-5. References.....	90
Chapter IV. Anti-reflective and anti-fogging film using mesoporous silica nanoparticles.....	91
IV-1. Introduction.....	92
IV-2. Experimental.....	94

IV-3. Results and discussion.....	98
IV-3-4. Conclusions.....	113
IV-3-5. References.....	114
국문요약.....	115

List of tables

Table I-1. Electronic structure and color of lanthanide(III) ions.

Table I-2. Representative mesoporous silica.

Table I-3. Synthesis of mesoporous silica, depending on the template type.

List of equations

Equation I-1. $R_1 = \{(n_{\text{air}} - n_c) / (n_{\text{air}} + n_c)\}^2 = R_2 = \{(n_c - n_s) / (n_c + n_s)\}^2$

Equation I-2. $n_c^2 = n_s$

Equation I-3. $2 n_c d_c = \lambda/2$

Equation I-4. $R_{ij} = |R_{ij}| \exp [-2 (\delta_i + \delta_j)]$

Equation I-5. $R_{\text{sum}} = R_{01} + R_{12} + R_{23} + R_{34} + \dots + R_{ns}$

Equation I-6. $(n_s / n_{\text{air}}) n_1^2 = n_2^2$

Equation I-7. $n_1 d_1 = n_2 d_2 = \lambda/4$

Equation I-8. $\gamma_s - \gamma_{sl} > 71.726 \text{ mJ/m}^2$

Equation I-9. $\cos \theta_m = r \cos \theta_i$

Equation I-10. $r = \text{actual surface area} / \text{projected surface area}$

List of figures

Figure I-1. Light reflection of the single layer coated substrate.

Figure I-2. Light reflection from the multi-layer coated substrate.

Figure I-3. (a) Schematic of the gradient refractive index layer and (b) the vertical profile of the refractive index. The solid line denotes the gradient refractive index layer and the dashed line denotes the discrete low refractive index single layer.

Figure I-4. Schematic of the sensitization mechanism of lanthanide(III) complexes. The solid arrows indicate radiative transitions and the dotted arrows indicate nonradiative internal conversions. S, T, ISC, and ET denote singlet, triplet, intersystem crossing, and energy transfer, respectively.

Figure I-5. Representative OLEDs. C, ETL, EL, HTL, and A denote the cathode, the electron transporting layer, the emitting layer, the hole transporting layer, and the anode, respectively.

Figure I-6. Schematic of the synthesis of hollow silica nanoparticles.

Figure I-7. Schematic of Young's model, where γ_s is the solid surface free energy, γ_l is the liquid surface free energy (liquid surface tension), γ_{sl} is the solid-liquid interfacial free energy, and θ is the equilibrium contact angle on a flat surface.

Figure I-8. Photo-induced hydrophilic effect of TiO₂. CB is the conduction band and VB is the valence band.

Figure I-9. Minimal roughness factors for achieving superhydrophilicity, for given intrinsic contact angles of materials.

Figure I-10. Minimal roughness factors for achieving superhydrophobicity, for given intrinsic contact angles of materials.

Figure I-11. (a) Light scattering from water droplets condensed on an uncoated surface, in a high-humidity condition. (b) Clear reflection from a superwetted water layer on an anti-fogging coated surface, in a high-humidity condition.

Figure II-1. Normalized absorption, excitation ($\lambda_{em} = 615$ nm) and emission ($\lambda_{ex} = 405$ nm) spectra of TDPP-Eu(III) in THF (10^{-2} mM) and transmitted white LED backlight spectrum of the LCD.

Figure II-2. Photographs of the uncoated glass (left) and the TDPP-Eu(III) coated glass (right) under visible light (a) and under near-UV light (b).

Figure II-3. Refractive indices of the films depending on TDPP-Eu(III) compositions.

Figure II-4. The emission of the Eu(III) complex ($\lambda_{ex} = 405$ nm) coated glass before and after UV irradiation.

Figure II-5. SEM images of (a) the surface and (b) the cross-section of the **LR-silica** layer. Scale bar is 100 nm for (a) and 50 nm for (b).

Figure II-6. (a) Calculated optimum thickness as a function of a refractive index. (b) Cross-sectional SEM image of the **AR-Eu** layer on the glass. Scale bar is 100 nm.

Figure II-7. Reflectance of the uncoated glass and the surface-coated glass. The calculated reflection spectra of the HR-Eu and LR-silica films on the glass were obtained considering their refractive indices of 1.57 and 1.34, respectively, and thicknesses of 85 and 100 nm, respectively. The calculated reflection spectrum of the AR-Eu film on the glass was obtained based on the bottom layer, with a refractive index of 1.57 and a thickness of 88 nm, and on the top layer with a refractive index of 1.37 and a thickness of 101 nm.

Figure II-8. Photographs of the uncoated display screen (left) and the **AR-Eu** coated display screen (right) under irradiation by an indoor fluorescent lamp.

Figure II-9. Photographs of the uncoated display screen (a) and the **AR-Eu** coated display screen (b) taken while using a 405 nm laser pointer.

Figure III-1. TEM imaging of hollow silica nanoparticles. The scale bar is 50 nm.

Figure III-2. Refractive index of a layer of hollow silica nanoparticles, with inter-particle pores.

Figure III-3. Refractive indices of hollow silica nanoparticles, calculated from the particles' core-shell volume fraction. The shell thicknesses are (a) 10 nm

and (b) 5 nm.

Figure III-4. (a) Refractive index and (b) reflectance of a coating layer, vs. the concentration of the hollow silica nanoparticles. The dashed line with circles: reflectance results for the glass substrate. The solid line with closed diamonds: reflectance results for the TAC substrate.

Figure III-5. Cross-sectional SEM images of UV curable hollow silica nanoparticle solution (HS-AR-30) on the (a) glass substrate and (b) TAC substrate. Scale bar is 1 μm .

Figure III-6. Si profiles for solutions of UV-curable hollow silica nanoparticles on (a) the glass substrate and (b) the TAC substrate, obtained by the EDS analysis.

Figure III-7. Calculated reflectance vs. the refractive indices of the coating layer on the TAC film with the refractive index of 1.47.

Figure III-8. Film SEM images for the solution with 30 wt% concentration of hollow silica nanoparticles coated on the TAC substrate: (a) for the EA to overall solvent ratio of 14 wt%, (b) for the EA to overall solvent ratio of 50 wt%, (c) for the EA to overall solvent ratio of 90 wt%. The scale bars in (a) and (b) are 1 μm , and that in (c) is 5 μm .

Figure III-9. Aggregation of hollow silica nanoparticles coated on the polymer substrate: (a) immediately after coating, (b) swelling of the substrate induced by

the solvent and penetration of the acrylate, (c) the final phase-separated structure.

Figure III-10. Reflectance of a TAC film coated with a several micrometers thick layer of HS-AR-30. The black solid line is the measured reflectance, the gray dotted line is the simulated reflectance for the film coated with the 2- μ m-thick coating layer with the refractive index of 1.34. The refractive index of the TAC film was 1.47.

Figure IV-1. FT-IR spectra of S-150 and MPS-150.

Figure IV-2. SAXS pattern of MPS-150.

Figure IV-3. SEM images of MPS-150. The scale bar is 500 nm.

Figure IV-4. TEM images of MPS-150.

Figure IV-5. Nitrogen adsorption-desorption isotherm for MPS-150.

Figure IV-6. BJH pore size distribution for MPS-150.

Figure IV-7. Surface roughness factor r vs. the intrinsic contact angle, calculated from the Wenzel equation.

Figure IV-8. SEM images of MPS-150 dispersion in (a) water and (b) DMF. The scale bar is 5 μ m.

Figure IV-9. Cross-sectional SEM image of MPS-150 dispersion in DMF. The scale bar is 500 nm.

Figure IV-10. SEM images of the coating surfaces with (a) MPS-150

dispersion in DMF, (b) AF-AR-80, (c) AF-AR-67, (d) AF-AR-50, (e) AF-AR-33, and (f) AF-AR-20, respectively. The scale bar is 1 μm and the magnification of all the images is the same.

Figure IV-11. Reflectance of the coating film, vs. the MPS-150 ratio.

Figure IV-12. Schematic illustration of haze.

Figure IV-13. Images and reflectance spectrum of the optimal anti-reflection film obtained by coating with solution 2.

Figure IV-14. Water contact angles of coating films, vs. the MPS-150 concentration.

Figure IV-15. Characterization of anti-fogging using images, for a (a) AF-AR-67 coated glass and (b) uncoated glass, and water contact angles for a (c) AF-AR-67 coated glass and (d) uncoated glass.

Figure IV-16. Coating film's hardness, vs. the MPS-150 concentration.

Chapter I.

Introduction

I-1. Anti-reflection

I-1-1. Principle of anti-reflection coating

Anti-reflection films^[1-5] have been the subject of extensive investigations since their discovery in 1817 by Fraunhofer, who produced anti-reflective coating by etching a surface in a sulfur and nitric acid vapor. Later, Rayleigh provided the first theoretical treatment of anti-reflective coating after observing an increase in the transmittance for tarnished glass.

Anti-reflection films are used in many applications, such as flat panel displays, solar cells, and optical lenses. The main mechanism of anti-reflection coating is the destructive interference of the light rays reflected from the surface and the light rays reflected from the interface between the coating layer and the substrate.^[6] To realize a perfect destructive interference of the two types of reflected light rays, two main conditions should be fulfilled. First, the intensities of the two reflections should be the same. Second, the phase difference between the two reflected light rays should be an odd multiple of $\lambda/2$, to ensure that the two light rays interfere destructively (out of phase). Scattering and absorption of light are assumed to be zero. In Figure I-1, the intensities of the reflected light rays, R_1 and R_2 , should be the same, and the phase difference should be an

odd multiple of $\lambda/2$. The values of R can be calculated from Fresnel's equation.

For normal incidence (angle of incidence equal to zero), these values are

$$R_1 = \left\{ \frac{(n_{\text{air}} - n_c)}{(n_{\text{air}} + n_c)} \right\}^2 = R_2 = \left\{ \frac{(n_c - n_s)}{(n_c + n_s)} \right\}^2 \quad (\text{Equation I-1})$$

where R_1 is the reflectance from the coating layer, R_2 is the reflectance from the interface between the coating layer and the substrate, and n_{air} , n_c , n_s are the refractive indices of air, the coating layer, and the substrate, respectively.

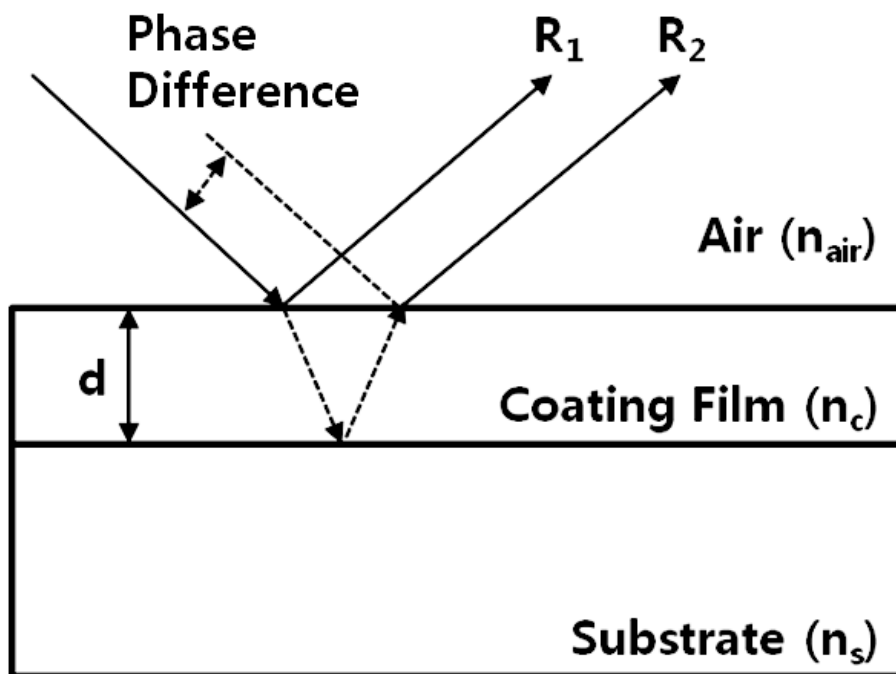


Figure I-1. Light reflection of the single layer coated substrate.

Because $n_{\text{air}} = 1$, Equation I-1 can be reduced to Equation I-2:

$$n_c^2 = n_s \quad (\text{Equation I-2})$$

The R_2 propagates through the coating layer, is reflected from the interface between the coating layer and the substrate, and is transmitted back to air through the coating layer. To ensure destructive interference between this ray and the one reflected from the coating surface, the phase difference between these rays should satisfy

$$2 n_c d_c = \lambda/2 \quad (\text{Equation I-3})$$

where d_c is the thickness of the coating layer and λ is the wavelength of the incident light.

For a glass substrate, with the refractive index of 1.5, the optimal refractive index was calculated as 1.22, and the optimal thickness of the coating layer was ~114 nm for the wavelength of 555 nm; this wavelength is the one to which our eyes are the most responsive. However, solid materials with intrinsic refractive indices as low as 1.22 are virtually nonexistent.^[7] Furthermore, the film thickness required for the destructive interference to occur depends on the

wavelength. As a result, a green light destructive coating on a glass reflects both relatively short and relatively long wavelengths in the visible range, which is manifested as purple-like reflection, contributed by both blue light and red light.

To overcome this problem, multi-layer coating is proposed. The main idea remains the same as for single-layer coating. The reflected light rays from all layers should add up to zero. In Figure I-2, R can be calculated by employing vector analysis, to account for intensities and phases of different light rays. The light reflected from the interface between the i-th and j-th layers, R_{ij} , is calculated as

$$R_{ij} = |R_{ij}| \exp [-2 (\delta_i + \delta_j)] \quad \text{(Equation I-4)}$$

where $|R_{ij}| = [(n_i - n_j)/(n_i + n_j)]$ and the phase difference is $\delta_i = 2\pi n_i d_i / \lambda$.

Therefore, the sum over reflectance contributions is

$$R_{\text{sum}} = R_{01} + R_{12} + R_{23} + R_{34} + \dots + R_{ns} \quad \text{(Equation I-5)}$$

In the case of two layers of anti-reflection coating, the intensity and phase differences are calculated from the following equations:

I-1-2. Fabrication of anti-reflection coating

Equation I-2 suggests that a low refractive index layer is necessary for anti-reflective coating. A structure with nanopores is a representative low refractive index layer. Because the refractive index of air is 1, the nanopores in such a structure effectively reduce the refractive index of the layer. The refractive index of a layer with nanopores can be calculated given the volume fraction of air and the material comprising the layer. Owing to these advantages of nanoporous structures, silica nanoparticles with porous structures have attracted considerable attention as a potential anti-reflection coating material. Rubner's group investigated anti-reflection films with layer-by-layer assembly of anionic silica nanoparticles and polycations.^[8,9] The refractive index of the obtained coating layer was as low as 1.22, resulting from the presence of nanopores between the constituent particles, and the coating layer exhibited superwetting properties owing to its nanoporosity. This group further studied the surface modification of the top layer of silica nanoparticles by hydrophobic silane. The modified structure exhibited superhydrophobic behavior with anti-reflection properties. Silica nanoparticles with intrinsic pores in their structure were also investigated. The group of Okubo fabricated anti-reflection films containing mesoporous silica nanoparticles.^[10] They achieved the minimal reflectance of

1.5% to 2.5% for a glass substrate with mesoporous silica nanoparticles treated with a trimethylsilyl group and siloxane oligomer. Wakefield's group prepared anti-reflection films containing mesoporous silica and TEOS as a binder.^[11] The achieved minimal reflectance was below 0.1% for light in the visible range, and the researchers were able to shift the minimal reflectance to the infrared range for solar cells and optical windows, by simply controlling the concentration and spin-coating conditions. Anti-reflection films with hollow silica nanoparticles were investigated by the groups of Cohen^[12] and Song.^[13] Cohen's group pre-synthesized hollow silica nanoparticles and fabricated anti-reflection films by layer-by-layer assembly on a PMMA substrate, whereas Song's group obtained anti-reflection films after calcination. They dipped a substrate into silica nanospheres containing PAA and subsequently into an acid catalyzed silica sol, and removed the PAA template by calcination.

Another approach is based on biomimetic nano-patterned structures that are inspired by the structures such as the moth eye and cicada wings. These biological structures exhibit anti-reflective characteristics owing to their highly ordered arrays of nano-pillars, which lead to the diffraction and interference of light rays.

The group of Samulski replicated the *Attacus atlas* moth compound eye using

a soft lithographic method.^[14] The reflectance of the replicated three-dimensional micro-lens arrays was under 1% for light in the visible range, as low as the real moth eye reflectance. Lim's group fabricated a moth eye structure with a nano-pillars array on glass.^[15] They investigated the dependence of the structure's optical properties on the morphology of the nano-pillars array. For a glass sample treated on both sides, the transmittance was above 99.5% and the reflectance was under 0.5%, for a specific wavelength. Wang's group replicated the cicada's wing structure using a photo-curable liquid perfluoropolyether mold and triacrylate.^[16] Owing to the low surface adhesion property of the perfluoropolyether mold, the cicada's wing structure was preserved and the final triacrylate layer could also be easily detached. The transmittance of this patterned triacrylate increased by 2.2% by integrating a sphere mode, owing to its anti-reflection characteristics. Chattopadhyay's group designed cicada-wing inspired nano-tip arrays, using both low refractive index and high refractive index materials.^[17] They simulated a structure with the reflectance of 1% and experimentally realized a hemispherical reflectance mode.

Alternatively, the method of the gradient refractive index has also been considered. By reducing the refractive index gradually, from the refractive index of the substrate to the refractive index of air, the reflectance was

minimized. Because reflection occurs at an interface between layers with different refractive indices, an ideal gradient refractive index layer exhibits no reflection (Figure I-3).

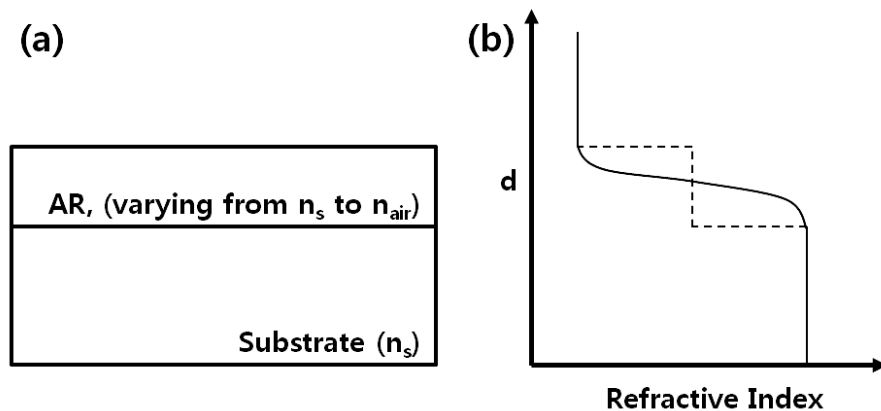


Figure I-3. (a) Schematic of the gradient refractive index layer and (b) the vertical profile of the refractive index. The solid line denotes the gradient refractive index layer and the dashed line denotes the discrete low refractive index single layer.

Han's group fabricated gradient refractive index coating by spin-coating the solution of a polystyrene-block-poly (methyl methacrylate) / PMMA blend onto an octadecyltrichlorosilane-modified glass substrate. In the vertical direction, the PMMA domains were phase-separated with the gradient distribution and were subsequently removed from the matrix.^[18] Graded refractive index

coatings have been studied for realizing gradient refractive index coatings. Using the RIE process, Miyata's group fabricated an assembly of pointed subwavelength structures composed of a mesoporous silica layer, and the mesopores were filled with a proper amount of titanium dioxide using low-pressure chemical vapor deposition.^[19] The layer with the matching refractive index demonstrated highly suppressed reflectance, whereas the hollow coating layer with the mismatched refractive index exhibited the reflectance higher than 1%, for a BK7 glass substrate. Xu's group fabricated a double-layered graded refractive index coating with silica.^[20] First, they prepared a layer with the refractive index of 1.34, containing mesoporous silica, by utilizing a sol-gel process, and over-coated the layer with silica nanoparticles that had the refractive index of 1.13. The peak transmittance of a double-layered stacked gradient refractive index coating film was ~100.0%, and the film transmittance in the visible range was above 99.6%.

I-2. Photoluminescent lanthanide(III) ions

I-2-1. The photoluminescence mechanism of lanthanide(III) ions

Lanthanide(III) ions have attracted significant attention owing to their optical characteristics.^[21-25] These ions have been used in various applications, such as optical and biological sensors, optical waveguides, electroluminescent materials for organic light-emitting diodes (OLEDs), and signal amplifiers for optical fibers. They exhibit a line-like narrow emission and long luminescence lifetime resulting from the intra-configurational f-f transition. The 4f orbitals of lanthanide(III) ions are gradually filled from $4f^0$ to $4f^{14}$ (Table I-1).^[26,27]

Depending on the type of the lanthanide ion, the emission color can be tuned from the ultraviolet (UV) to the near infrared (NIR) region, including the visible region. In the visible region, Tm(III), Tb(III), Dy(III), Sm(III), and Eu(III) ions emit blue, green, yellow, orange, and red light, respectively.

However, lanthanide(III) ions have low absorption coefficients, which makes it difficult to directly excite these ions. To overcome this disadvantage, Weissman studied the luminescence of lanthanide complexes with organic ligands.^[28] Owing to the intense absorption of organic ligands, a significantly

larger amount of energy can be transferred to lanthanide ions by the intramolecular energy transfer mechanism that has been termed the antenna effect or sensitization.^[29] Crosby and Whan proposed the energy transfer mechanism for lanthanide complexes (Figure I-4).^[30-32]

Table I-1. Electronic structure and color of lanthanide(III) ions.

Element (Symbol)	Configuration Ln ³⁺	Ground State	Color in aq. solution
lanthanum (La)	[Xe]4f ⁰	¹ S ₀	colorless
cerium (Ce)	[Xe]4f ¹	² F _{5/2}	colorless
praseodymium (Pr)	[Xe]4f ²	³ H ₄	yellow-green
neodymium (Nd)	[Xe]4f ³	⁴ I _{9/2}	lilac
promethium (Pm)	[Xe]4f ⁴	⁵ I ₄	pink
samarium (Sm)	[Xe]4f ⁵	⁶ H _{5/2}	pale yellow
europium (Eu)	[Xe]4f ⁶	⁷ F ₀	colorless
gadolinium (Gd)	[Xe]4f ⁷	⁸ S _{7/2}	colorless
terbium (Tb)	[Xe]4f ⁸	⁷ F ₆	colorless
dysprosium (Dy)	[Xe]4f ⁹	⁶ H _{15/2}	pale yellow
holmium (Ho)	[Xe]4f ¹⁰	⁵ I ₈	yellow
erbium (Er)	[Xe]4f ¹¹	⁴ I _{15/2}	pink
thulium (Tm)	[Xe]4f ¹²	³ H ₆	pale green
ytterbium (Yb)	[Xe]4f ¹³	² F _{7/2}	colorless
lutetium (Lu)	[Xe]4f ¹⁴	¹ S ₀	colorless

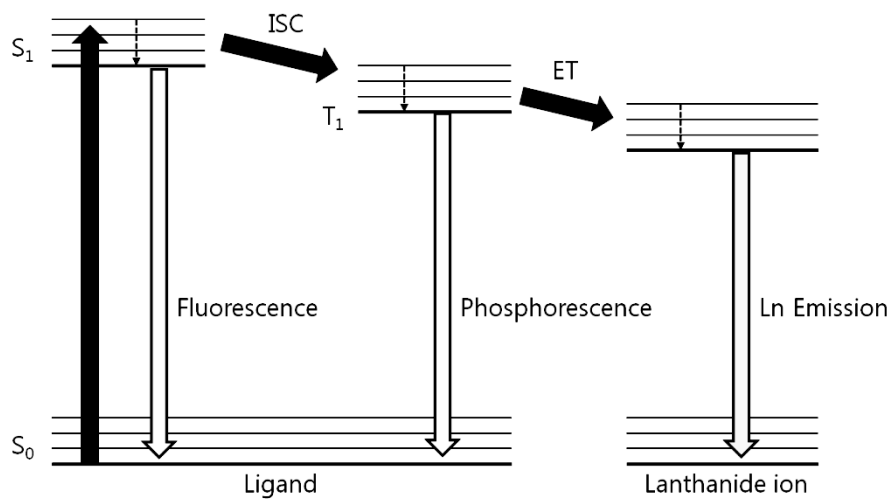


Figure I-4. Schematic of the sensitization mechanism of lanthanide(III) complexes. The solid arrows indicate radiative transitions and the dotted arrows indicate nonradiative internal conversions. S, T, ISC, and ET denote singlet, triplet, intersystem crossing, and energy transfer, respectively.

When lanthanide(III) complexes are irradiated by light, the organic ligands of these complexes are excited to the first excited singlet energy state (S_1). In the internal conversion process, the excited ligands readily relax to the lowest vibrational level associated with the S_1 state. Then, the excited singlet state can be deactivated via either a radiative or nonradiative transition. The radiative deactivation yields fluorescence, whereas the nonradiative deactivation proceeds via the intersystem crossing (ISC), which generates the first excited triplet state (T_1). The excited triplet state T_1 also undergoes fast relaxation to the

lowest vibrational level and is deactivated radiatively or nonradiatively. The radiative deactivation from the triplet state yields phosphorescence by the spin-forbidden transition, which is characterized by a long lifetime and a significant Stokes shift. Meanwhile, the energy can be transferred to the excited state of lanthanide(III) ions via the photon-assisted pathway in the process of the nonradiative deactivation. Through this energy transfer process lanthanide(III) ions can be excited indirectly, and can be deactivated radiatively or nonradiatively. The final radiative deactivation from the excited state to the lower 4f state yields characteristic line-like photoluminescence.

To increase the luminescence efficiency of lanthanide(III) ions, facilitation of the energy transfer and suppression of the nonradiative deactivation are needed. Because the distance between the ligand molecules and the metal ions is critical to the energy transfer, the location of the light-absorbing group of the ligand strongly determines the luminescence efficiency. Higher emission efficiency of a lanthanide(III) complex can be achieved by decreasing the distance from the chromophore group of the ligand molecules to the lanthanide(III) ions.

On the other hand, the excitation energy can be dissipated owing to bond vibrations, collisions with solvent molecules, or energy back transfer processes, reducing the luminescence efficiency. To minimize these unfavorable effects,

appropriate organic ligand molecules and coordination design are necessary.

I-2-2. Applications of photoluminescent lanthanide(III) ions

Owing to their characteristic photoluminescence properties, lanthanide(III) ions have been used in various optical applications. A UV-sensitive ink featuring europium(III) β -diketonate complexes was used as a countermeasure for counterfeiting banknotes and other valuable papers. This ink is invisible under the visible light irradiation but emits red light under the UV light irradiation. Meijerink's group speculated that red-emitting fibers and patterns of UV-irradiated euro banknotes resulted from the presence of europium(III) β -diketonate complexes.^[33] The efficiency of silicon solar cells was improved by applying europium(III) and terbium(III)-doped ormosil glass films on photovoltaic devices. The lanthanide(III)-doped ormosil glass films absorbed UV light and emitted visible light, increasing the absorption efficiency of silicon solar cells.^[34,35] Light-converting properties were also used for fabricating films in agriculture applications.^[36] Ranita company commercialized polymer films (Redlight) containing inorganic europium(III)-containing compounds (Ksanta) for use in greenhouses. The yield of plants grown in such greenhouses increased by up to a 100% owing to the Polysvetan effect.^[37,38]

Erbium(III) ions are among the lanthanide(III) ions that are used in telecommunication applications. Erbium(III) ions exhibit emission at the wavelength of 1540 nm, which matches well the range of wavelengths for telecommunication applications. Erbium(III) ions are used as optical amplifiers in optical fiber cores and can be excited by external laser sources. Their stimulated emission at 1540 nm amplifies the optical fiber signal.^[39]

Lanthanide(III) ions have been considered as electroluminescent materials for OLEDs. Since the 1963 discovery by Pope of organic electroluminescence, OLEDs have been used in displays and lighting fixtures. Their simple and thin structure makes them very suitable for mobile and flexible displays. The different types of OLED structures are shown in Figure I-5.

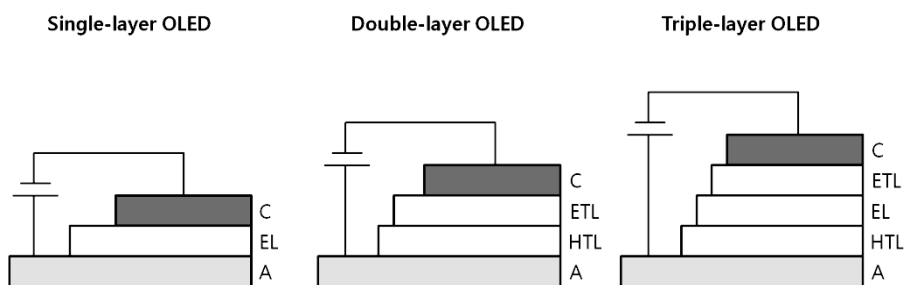


Figure I-5. Representative OLEDs. C, ETL, EL, HTL, and A denote the cathode, the electron transporting layer, the emitting layer, the hole transporting layer, and the anode, respectively.

Theoretically, emitting layers containing lanthanide(III) ions are advantageous for color saturation and emission efficiency of OLEDs. Because broad emission bands exhibit dull colors that decrease color saturation, monochromatic lanthanide(III) ions with narrow emission bands (with full width at half maxima under 10 nm) can effectively increase the color saturation.

In spin statistics, hole and electron recombinations make 75% of triplet excitons and 25% of singlet excitons, and only singlet excitons can yield electroluminescence, which means the emission efficiency of OLEDs is in general limited to 25%. However, the emission efficiency of OLEDs can be improved by incorporating lanthanide(III) ions, because the excitation energy of triplet excitons can also be transferred to the incorporated lanthanide(III) ions, increasing the luminescence. In first-generation devices, the luminance of OLEDs based on the europium(III) compound was quite low, 0.3 cd/m².^[40] By optimizing organic ligands, the luminance of red-emitting OLEDs was improved up to 1670 cd/m².^[41]

Lanthanide(III) complexes are also used as chemical sensors. Eu(tta)₃(phen) exhibits luminescent quenching by oxygen molecules; therefore, it can be used for monitoring the oxygen concentration by reporting the luminescence intensity.^[42] A sol-gel glass matrix with Tb-DOTA complexes bearing an N-

methylphenanthridinium chromophore was also considered as an oxygen concentration sensor.^[43] Studies of pH sensing and anion sensing using lanthanide(III) complexes were also reported.^[44,45]

I-3. Porous silica nanoparticles

I-3-1. Synthetic method of obtaining mesoporous silica nanoparticles

Silica nanoparticles with pores have been widely investigated owing to their unique optical and physical properties. Mesoporous silica nanoparticles are representative porous silica, and have been used in many applications, such as sensors, catalytic materials, adsorbents, nano-reactors, separation systems, and drug delivery systems. In optical applications, mesoporous silica nanoparticles have been of great interest as low refractive index materials for anti-reflection coatings, owing to their highly porous structures.

Since several groups had synthesized mesoporous silica in 1990s, various synthesis methods have been proposed.^[46-50] Properties and morphologies of synthesized mesoporous silica depend on the silica source, template, and catalysis. Some representative mesoporous silica nanoparticles are summarized in Table I-2. Mesoporous silica nanoparticles are typically synthesized as follows. First, an inorganic silica source material containing template molecules is hydrolyzed and condensed in a specific pH condition. In the final stage, the template molecules are removed by calcination or extraction.

Table I-2. Representative mesoporous silica.

Abbreviation	Full Name	Ref.
MCM	Mobil Crystalline Matter	[47,48]
SBA	Santa Barbara Amorphous	[49,50]
MSU	Michigan State University	[51]
AMS	Anionic surfactant templated Mesopous Silca	[52]
FDU	Fudan University	[53]
FSM	Foled Sheet Mesoporus	[54]
HMS	Hexagonal Mesopous Silica	[55]
IBN	Institute of Boiengineering and Technology	[56]
KIT	Korea Advanced Institute of Science and Technology	[57]
MCF	Meso Cellular Foam	[58]
TUD	Technische University Deft	[59]

The template molecules function as structure-directing agents, critically defining the morphology and final structure of mesoporous silica nanoparticles. Various surfactants have been investigated as templates for mesoporous nanoparticles, owing to their amphiphilic molecular structures. Mesoporous silica nanoparticles are listed in Table I-3, considering the surfactants and synthesis conditions.

Table I-3. Synthesis of mesoporous silica, depending on the template type.

Template	Route	Symbol	Condition	Example
Cationic	S^+I^-	S^+ : cationic surfactant I^- : anionic silicate species	basic	MCM-41, MCM-48, MCM-50, SBA-6 ^[60] , SBA-8 ^[61] , FDU-11, FDU-13 ^[62]
	S^+XI^+	S^+ : cationic surfactant X^- : Cl^- , Br^- I^+ : silicate species	acidic	SBA-1 ^[63] , SBA-2 ^[64] , SBA-3 ^[65]
Anionic	S^-I^+	S^- : anionic surfactant I^+ : transition metal ion	Neutral -basic	Mesopous aluminum, iron, lead oxide
	$S^-M^+I^-$	S^- : anionic surfactant M^+ : Na^+ , K^+ I^- : transition metal ion	basic	W, Mo oxide ^[66]
Nonionic	S^0I^0	S^0 : nonionic surfactant I^0 : silicate species	neutral	HMS, MSU ^[67]
	$S^0H^+XI^+$	S^0 : nonionic surfactant X^- : Cl^- , Br^- I^+ : silicate species	acidic	SBA-11, SBA-15, SBA-16, FDU-5, FDU-12, KIT-5 ^[68]

Hexadecyltrimethylammonium bromide (CTAB) is the most famous cationic surfactant. For anionic surfactants, anionic phosphate surfactants, carboxylates, sulfates, and sulfonates have been widely used. Representative nonionic surfactants are three block copolymers such as the ones in the Pluronic series.

I-3-2. Synthesis of hollow silica nanoparticles

Hollow silica nanoparticles are another representative porous silica materials. Hollow silica nanoparticles have an empty core and thin shell made of silica, which yields very low refractive indices. There are two main strategies to synthesize hollow silica nanoparticles (Figure I-6).

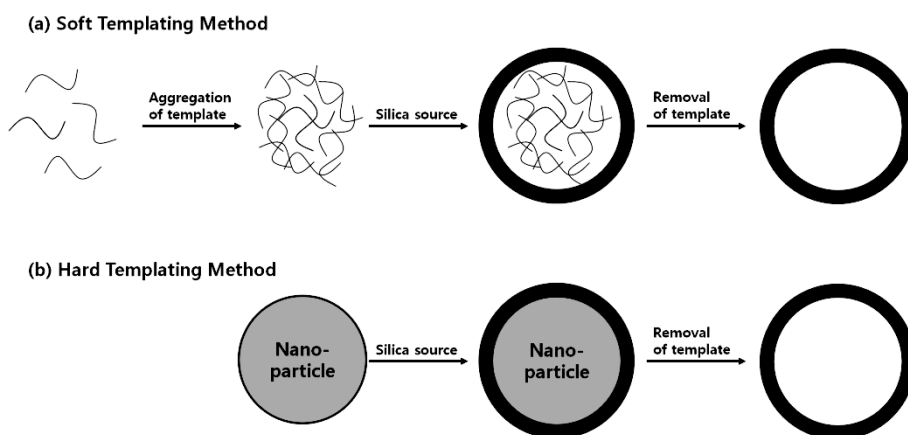


Figure I-6. Schematic of the synthesis of hollow silica nanoparticles.

Soft templating methods have also been considered. In this approach, droplets of polymer templates are formed in an oil-water emulsion and silica sources are deposited around the droplets. The deposited silica sources are converted into silica shells, and the template molecules in the core are removed by calcination or extraction. Yu's group synthesized hollow silica spheres using polyelectrolytes.^[69] Poly(acrylic acid) was used for forming a spherical colloidal aggregation in an ethanol solution, and subsequent hydrolysis of TEOS under control of ammonia induced formation of thin walls of silica around the poly(acrylic acid). Finally, the poly(acrylic acid) was removed by solvent washing. Fan's group fabricated hollow silica spheres using thermosensitive poly(*N*-isopropylacrylamide) (PNIPAm).^[70] PNIPAm was used as a reversible template owing to its thermosensitivity. PNIPAm chains can reversibly aggregate and dissolve in an aqueous solution. By increasing the temperature, PNIPAm chains aggregate and act as a soft template core for hollow silica, and they can be easily removed by lowering the temperature as they dissolve and can be extracted from the hollow silica core. In addition, the extracted PNIPAm can aggregate repeatedly and can be used as a recyclable template.

Another strategy of synthesizing hollow silica nanoparticles utilizes the

method of hard templating. Polystyrene (PS) nanoparticles are typical hard templates for hollow silica nanoparticles. In the hard templating approach, the template's size can be controlled precisely and the size distribution of synthesized hollow silica nanoparticles is satisfactory, whereas hollow silica nanoparticles synthesized using soft templating methods exhibit relatively broad size distributions. Blanco's group synthesized mono-dispersed silica hollow spheres using PS spheres.^[71] PS spheres were synthesized and silica coating was applied on the PS spheres, after which the PS spheres were removed by solvent extraction and subsequent calcination or simply in one-step calcination process without solvent extraction.

I-4. Superhydrophilicity

I-4-1. Definition and mechanism of superhydrophilicity

Accompanied by a growing interest in superhydrophobicity and superhydrophobic surfaces, significant research on superhydrophilicity and superwetting surfaces has been conducted during the last twenty years. Since Onda et al. investigated the wettability of fractal surfaces, highly water-wetting surfaces became known as superwetable surfaces.^[72,73] The concept of superhydrophilicity was introduced by several Japanese research groups in 2000.^[74-77] In the literature, a superhydrophilic surface is defined as a surface with the water contact angle smaller than 5° , whereas a surface with the water contact angle larger than 150° is called a superhydrophobic surface. A leaf of lotus, which exhibits an excellent water repelling property, is a representative naturally occurring superhydrophobic surface, and its mechanism was investigated by Barthlott and Neinhuis.^[78] Fujishima's group was the first to study highly hydrophilic surfaces.^[79] They achieved a nearly 0° water contact angle for a titanium dioxide surface irradiated by UV light.

Superhydrophilic surfaces are characterized by anti-fogging, ultrafast drying, and self-cleaning ability. The relationship between the surface and interface

energy of different materials and the contact angle of a liquid on a flat solid surface is shown in Figure I-7.

$$\gamma_s = \gamma_{sl} + \gamma_l \cos\theta$$

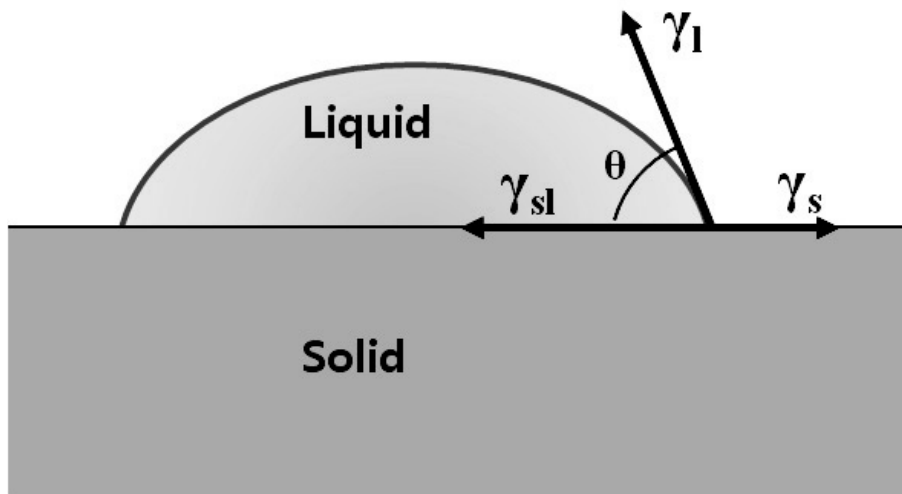


Figure I-7. Schematic of Young's model, where γ_s is the solid surface free energy, γ_l is the liquid surface free energy (liquid surface tension), γ_{sl} is the solid-liquid interfacial free energy, and θ is the equilibrium contact angle on a flat surface.

To obtain a superhydrophilic surface, the water contact angle should be smaller than 5° , which implies $\cos(\theta) > 0.996$. By considering the surface

energy of water (72 mJ/m^2) and the boundary condition of Young's equation, the equation can be expressed as

$$\gamma_s - \gamma_{sl} > 71.726 \text{ mJ/m}^2 \quad (\text{Equation I-8})$$

The surface free energy of the solid should be high and at the same time the solid-liquid interfacial free energy should be minimal, which means that the solid surface should be highly hydrophilic for achieving superhydrophilicity.

Several strategies for fabricating superhydrophilic surfaces have been considered. Specific metal oxides, such as TiO_2 , ZnO , SnO_2 , WO_3 , and V_2O_5 , are superhydrophilic under the UV irradiation, resulting in the photo-induced hydrophilic effect, which was discovered accidentally at the Japanese company TOTO in 1995.^[79] TiO_2 can generate electrons and holes under the UV irradiation, which induces Ti^{3+} defect sites and oxygen vacancies respectively, following which water molecules are adsorbed on the TiO_2 surface, resulting in superhydrophilicity. The same mechanism explains the superhydrophilicity of ZnO . Figure I-8 schematically shows the photo-induced hydrophilic effect.^[80]

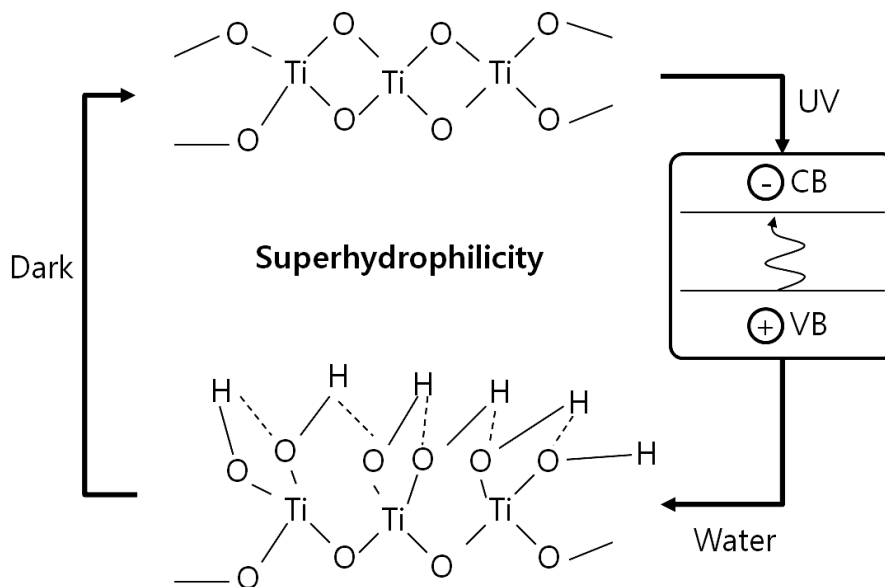


Figure I-8. Photo-induced hydrophilic effect of TiO₂. CB is the conduction band and VB is the valence band.

However, the photo-induced hydrophilic effect of TiO₂ decays with time in a dark environment, and a superhydrophilic surface becomes a hydrophilic surface. Although the superhydrophilicity property can be recovered reversibly, permanently superhydrophilic surfaces have been investigated using a different strategy.

Another representative approach to superhydrophilicity is surface roughening of hydrophilic materials. In 1936, Wenzel defined the relationship between the wettability and roughness of a surface as follows.^[81]

$$\cos \theta_m = r \cos \theta_i \quad (\text{Equation I-9})$$

where θ_m , r , and θ_i denote the macroscopic contact angle, the roughness factor, and the intrinsic contact angle, respectively.

The roughness factor r is defined as the ratio of the actual to the projected solid surface area (Equation I-10):

$$r = \text{actual surface area} / \text{projected surface area} \quad (\text{Equation I-10})$$

The roughness factor of an ideally flat surface is 1, because the actual surface area and the projected surface area are the same. However, the roughness factor of a rough surface is larger than 1. For a fixed dimensional area, the actual surface area increases with increasing the surface roughness, whereas the projected surface area does not change. As a result, the roughness factor increases as the surface roughness of a solid increases.

According to Equation I-9, the macroscopic water contact angle can be increased or decreased by increasing the roughness factor. A surface with the intrinsic contact angle under 90° can demonstrate a smaller macroscopic contact angle compared with its intrinsic contact angle as the roughness factor increases.

Figure I-9 shows the minimal roughness factors needed for superhydrophilicity (water contact angle smaller than 5°) for given intrinsic contact angles of materials. The surfaces in the area below the line are superhydrophilic.

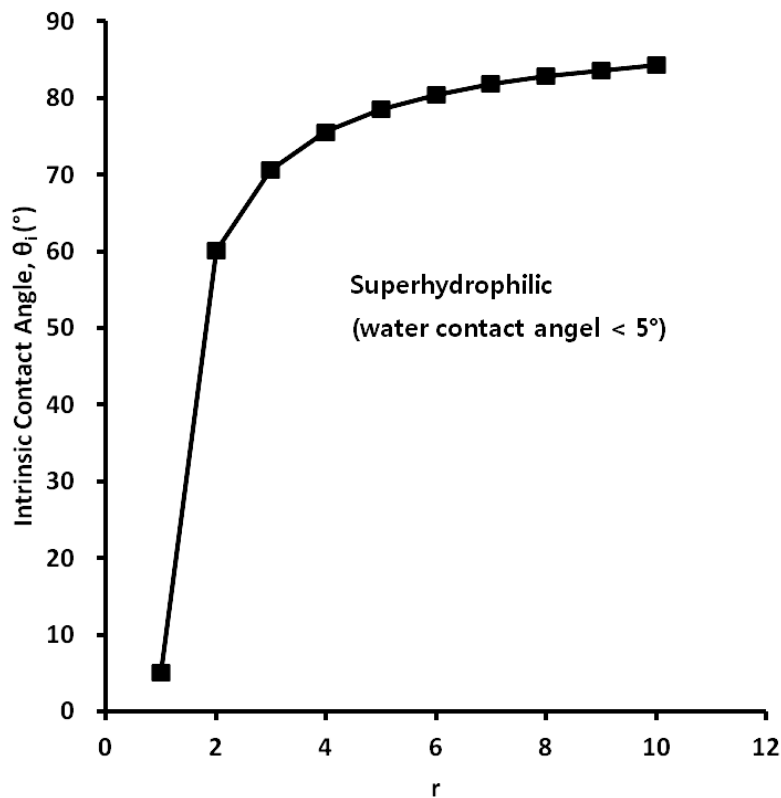


Figure I-9. Minimal roughness factors for achieving superhydrophilicity, for given intrinsic contact angles of materials.

On the other hand, a surface with the intrinsic contact angles larger than 90°

can exhibit a larger macroscopic contact angle than its intrinsic contact angle as the roughness factor increases. Figure I-10 shows the minimal roughness factors needed for superhydrophobicity (water contact angle larger than 150°) for given intrinsic contact angles of materials. The surfaces in the area above the line are superhydrophobic.

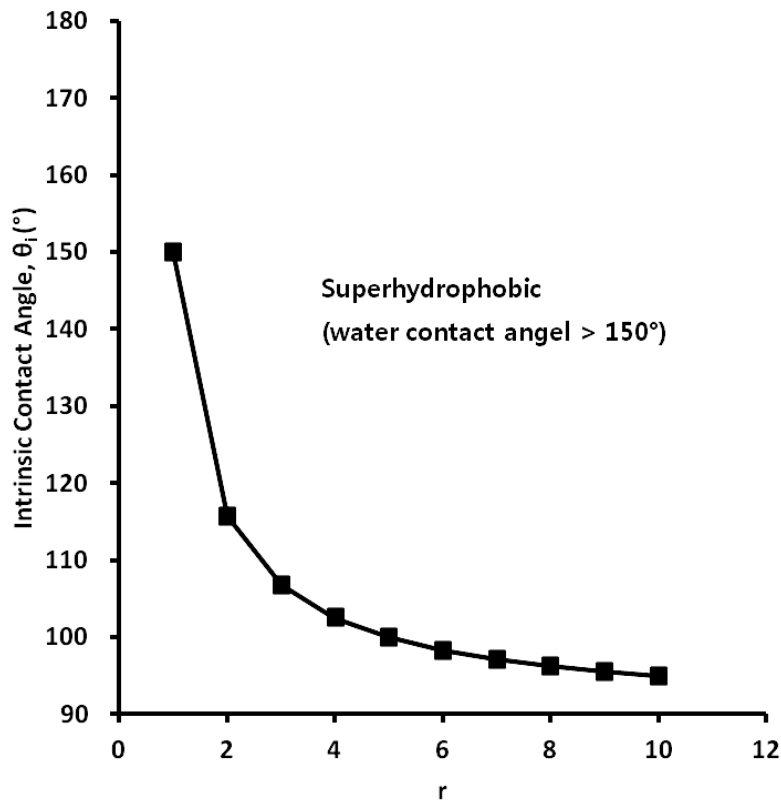


Figure I-10. Minimal roughness factors for achieving superhydrophobicity, for given intrinsic contact angles of materials.

Reversible superhydrophilic-superhydrophobic coatings have been of significant interest owing to their usability in sensors, microfluidics, and drug delivery. Reversible wettability can be accomplished on rough surfaces by reversibly altering chemical composition using external stimuli. Zhang and coworkers fabricated pH-sensitive reversible wetting surfaces by synthesizing a pH-sensitive polymer and applied it to a rough gold substrate. As the conformation of the pH-sensitive polymer changed depending on the pH value, the surface wettability of the coating was changed from superhydrophilic to superhydrophobic.^[90]

I-4-2. Applications of superhydrophilicity

Superhydrophilicity is utilized in many fields. Anti-fogging coating is one representative application of superhydrophilicity.^[91-95] Anti-fogging coated surfaces can diminish light scattering of the condensed water droplet on the surfaces under high humidity conditions owing to the surfaces' superwetting properties. (Figure I-11) Swimming goggles, optical lenses, and display screens coated with anti-fogging coatings can maintain optical clarity in high-humidity conditions.

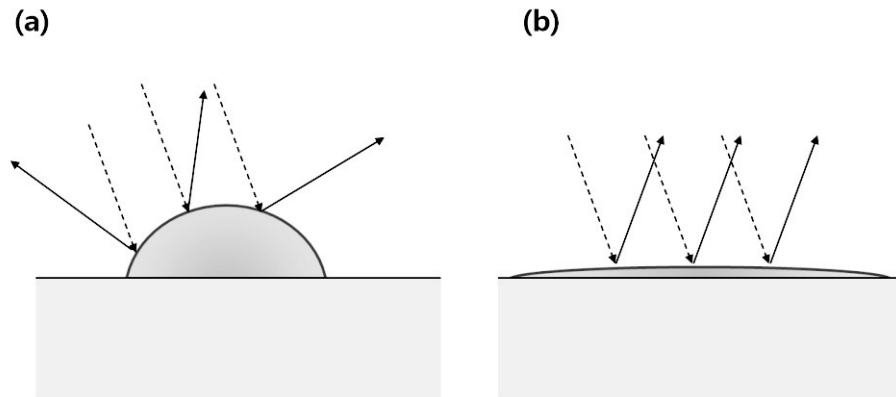


Figure I-11. (a) Light scattering from water droplets condensed on an uncoated surface, in a high-humidity condition. (b) Clear reflection from a superwetted water layer on an anti-fogging coated surface, in a high-humidity condition.

Superhydrophilicity can be also utilized in bio-fouling applications. Meng's group investigated the anti-fouling effect of superhydrophilic surfaces.^[96] Superhydrophilically treated surfaces demonstrated lower fouling by fluorescein and fluorescent proteins.

Optical fiber-based humidity sensors with superhydrophilic silica coating have also been fabricated.^[97] The fabricated sensors exhibited a rapid response time and good sensing linearity for relative humidity in the 40–98% range. Superhydrophilic anti-reflection films have been applied to solar cells, increasing their efficiency.^[98]

I-5. References

1. S. Chattopadhyay, Y. F. Huang, Y. J. Jen, A. Ganguly, K. H. Chen and L. C. Chen, *Mater. Sci. Eng., R*, 2010, **69**, 1.
2. J. Cai and L. Qi, *Mater. Horiz.*, 2015, **2**, 37.
3. X. Li, X. Yu and Y. Han, *Mater. Chem. C*, 2013, **1**, 2266.
4. H. K. Raut, V. A. Ganesh, A. S. Nair and S. Ramakrishna, *Energy Environ. Sci.*, 2011, **4**, 3779.
5. P. Buskens, M. Burghoorn, M. C. D. Mourad and Z. Vroon, *Langmuir*, 2016, **32**, 6781.
6. H. A. Macleod, in *Thin-film Optical Filters*, McGraw Hill, USA, 1989.
7. E. F. Schubert, J. K. Kim and J. -Q. Xi, *phys. stat. sol. (b)*, 2007, **244**, 3002.
8. F. C. Cebeci, Z. Wu, L. Zhai, R. E. Cohen and M. F. Rubner, *Langmuir*, 2006, **22**, 2856.
9. J. Bravo, L. Zhai, Z. Wu, R. E. Cohen and M. F. Rubner, *Langmuir*, 2007, **23**, 7293.
10. Y. Hoshikawa, H. Yabe, A. Nomura, T. Yamaki, A. Shimojima and T. Okubo, *Chem. Mater.*, 2010, **22**, 12.
11. J. Moghal, J. Kobler, J. Sauer, J. Best, M. Gardener, A. A.R. Watt and G. Wakefield, *ACS Appl. Mater. Interfaces*, 2012, **4**, 854.

12. Y. Du, L. E. Luna, W. S. Tan, M. F. Rubner and R. E. Cohen, *ACS Nano*, 2010, **4**, 4308.
13. X. Zhang, P. Lan, Y. Lu, J. Li, H. Xu, J. Zhang, Y. Lee, J. Y. Rhee, K. Choy and W. Song, *ACS Appl. Mater. Interfaces*, 2014, **6**, 1415.
14. D. Ko, J. R. Tumbleston, K. J. Henderson, L. E. Euliss, J. M. DeSimone, R. Lopez and E. T. Samulski, *Soft Matter*, 2011, **7**, 6404.
15. S. Ji, J. Park and H. Lim, *Nanoscale*, 2012, **4**, 4603.
16. X. Zhang, D. Ji, T. Lei, B. Zhao, K. Song, W. Hu, J. Wang, J. Pei and Y. Wang, *J. Mater. Chem. A*, 2013, **1**, 10607.
17. Y. Huang, Y. Jen, L. Chen, K. Chen and S. Chattopadhyay, *ACS Nano*, 2015, **9**, 301.
18. B. X. Li, J. Gao, L. Xue and Y. Han, *Adv. Funct. Mater.*, 2010, **20**, 259.
19. S. Kitamura, Y. Kanno, M. Yatanabe, M. Takahashi, K. Kuroda and H. Miyata, *ACS Photonics*, 2014, **1**, 47.
20. J. Sun, X. Cui, C. Zhang, C. Zhang, R. Ding and Y. Xu, *J. Mater. Chem. C*, 2015, **3**, 7187.
21. A.J. Kenyon, *Prog. Quantum Electron*, 2002, **26**, 225.
22. G. Blasse, *Prog. Solid State Chem.*, 1988, **18**, 79.
23. M. Elbanowski and B. J. Makowsaka, *Photochem. Photobiol. A*, 1996, **99**, 85.

24. Y. Hasegawa, Y. Wada and S. Yanagida, *J. Photochem. Photobiol. C*, 2004, **5**, 183.
25. B. M. Tissue, *Chem. Mater.*, 1998, **10**, 2837.
26. K. Binnemans, *Chem. Rev.*, 2009, **109**, 4283.
27. K. Binnemans and C. Görrler-Walrand, *Chemical Physics Letters*, 1995, **235**, 163.
28. S. I. Weissman, *J. Chem. Phys.*, 1942, **10**, 214.
29. J. R. Holst and A. I. Cooper, *Adv. Mater.*, 2010, **22**, 5212.
30. R. E. Whan and G. A. Crosby, *J. Mol. Spectrosc.*, 1962, **8**, 315.
31. G. A. Crosby, R. E. Whan and R. M. Alire, *J. Chem. Phys.*, 1961, **34**, 743.
32. G. A. Crosby, R. E. Whan and J. J. Freeman, *J. Phys. Chem.*, 1962, **66**, 2493.
33. J. F. Suyver and A. Meijerink, *Chem. Weekbl.*, 2002, **98**, 12.
34. H. Li, S. Inoue, D. Ueda, K. Machida and G. Adachi, *Electrochem. Solid State Lett.*, 1999, **2**, 354.
35. H. Li, S. Inoue, K. Machida and G. Adachi, *J. Electrochem. Soc.*, 1997, **144**, 4054.
36. C. Edser, *Plast., Addit. Compd.*, 2002, **4**, 20.
37. R. N. Shchelokov, *Vestnik. Acad. Nauk USSR*, 1986, **10**, 50.
38. V. S. Raida, A. E. Ivanitskii, A. V. Bushkov, O. S. Andrienko and G. A. Tolstikov, *Atmos. Oceanic Opt.*, 2003, **16**, 1029.

39. P. G. Kik and A. Polman, *MRS Bull.*, 1998, **23**, 48.
40. J. Kido, K. Nagai, Y. Okamoto and T. Skotheim, *Chem. Lett.*, 1991, **1267**.
41. P. P. Sun, J. P. Duan, J. J. Lih and C. H. Cheng, *Adv. Funct. Mater.*, 2003, **13**, 683.
42. Y. Amao, I. Okura and T. Miyashita, *Bull. Chem. Soc. Jpn.*, 2000, **73**, 2663.
43. S. Blair, R. Katakya, and D. Parker, *New J. Chem.*, 2002, **26**, 530.
44. A. Lobnik, N. Majcen, K. Niederreiter and G. Uray, *Sens. Actuators B*, 2001, **74**, 200.
45. K. L. Wong, G. L. Law, Y. Y. Yang and W. T. Wong, *Adv. Mater.*, 2006, **18**, 1051.
46. T. Yanagisawa, T. Shimizu, K. Kuroda and C. Kato, *Bull. Chem. Soc. Jpn.*, 1990, **63**, 988.
47. C. T. Kresge, M. E. Leonowicz, W. J. Roth, J. C. Vartuli and J. C. Beck, *Nature*, 1992, **359**, 710.
48. J. S. Beck, J. C. Vartuli, W. J. Roth, M. E. Leonowicz, C. T. Kresge, K. D. Schmitt, C. T. W. Chu, D. H. Olson, E. W. Sheppard, S. B. McCullen, J. B. Higgins and J. L. Schlenker, *J. Am. Chem. Soc.*, 1992, **114**, 10834.
49. D. Zhao, J. Feng, Q. Huo, N. Melosh, G. H. Fredrickson, B. F. Chmelka and G. D. Stucky, *Science*, 1998, **279**, 548.
50. D. Zhao, Q. Huo, J. Feng, B. F. Chmelka and G. D. Stucky, *J. Am. Chem.*

- Soc.*, 1998, **120**, 6024.
51. S. A. Bagshaw, E. Prouzet and T. J. Pinnavaia, *Science*, 1995, **269**, 1242.
52. S. Che, A. E. Garcia-Bennett, T. Yokoi, K. Sakamoto, H. Kunieda, O. Terasaki and T. Tatsumi, *Nat. Mater.*, 2003, **2**, 801.
53. C. Yu, Y. Yu and D. Zhao, *Chem. Commun.*, 2000, 575.
54. S. Inagaki, Y. Fukushima and K. Kuroda, *J. Chem. Soc. Chem. Commun.*, 1993, 680.
55. P. T. Tanev, M. Chibwe and T. J. Pinnavaia, *Nature*, 1994, **368**, 321.
56. Y. Han and J. Y. Ying, *Angew. Chem., Int. Ed.*, 2005, **44**, 288.
57. R. Ryoo, J. M. Kim, C. H. Ko and C. H. Shin, *J. Phys. Chem.*, 1994, **100**, 17718.
58. P. Schmidt-Winkel, W. W. Lukens, D. Zhao, P. Yang, B. F. Chmelka and G. D. Stucky, *J. Am. Chem. Soc.*, 1999, **121**, 254.
59. J. C. Jansen, Z. Shan, L. Marchese, W. Zhou, N. v. d. Puil and Maschmeyer, *Chem. Commun.*, 2001, 713.
60. Y. Sakamoto, M. Kaneda, O. Terasaki, D. Y. Zhao, J. M. Kim, G. Stucky, H. J. Shim and R. Ryoo, *Nature*, 2000, **408**, 449.
61. D. Y. Zhao, Q. S. Huo, J. L. Feng, J. M. Kim, Y. J. Han and G. D. Stucky, *Chem. Mater.*, 1999, **11**, 2668.
62. S. D. Shen, A. E. Garcia-Bennett, Z. Liu, Q. Y. Lu, Y. F. Shi, Y. Yan, C. Z.

- Yu, W. C. Liu, Y. Cai, O. Terasaki and D. Y. Zhao, *J. Am. Chem. Soc.*, 2005, **127**, 6780.
63. Q. S. Huo, D. I. Margolese, U. Ciesla, P. Y. Feng, T. E. Gier, P. Sieger, R. Leon, P. M. Petroff, F. Schuth, G. D. Stucky, *Nature*, 1994, **368**, 317.
64. Q. S. Huo, R. Leon, P. M. Petroff and G. D. Stucky, *Science*, 1995, **268**, 1324.
65. Q. S. Huo, D. I. Margolese and G. D. Stucky, *Chem. Mater.*, 1996, **8**, 1147.
66. J. Y. Ying, C. P. Mehnert and M. S. Wong, *Angew. Chem. Int. Ed.*, 1999, **38**, 56.
67. P. T. Tanev and T. J. *Science*, 1995, **267**, 865.
68. F. Kleitz, D. N. Liu, G. M. Anilkumar, I. S. Park, L. A. Solovyov, A. N. Shmakov and R. Ryoo, *J. Phys. Chem. B*, 2003, **107**, 14296.
69. Y. Wan and S. Yu, *J. Phys. Chem. C*, 2008, **112**, 3641.
70. B. Du, Z. Cao, Z. Li, A. Mei, X. Zhang, J. Nie, J. Xu and Z. Fan, *Langmuir*, 2009, **25**, 12367.
71. M. N. Gorsd, L. R. Pizzio and M. N. Blanco, *Procedia Materials Science*, 2015, **8**, 567.
72. T. Onda, S. Shibuichi, N. Satoh and K. Tsujii, *Langmuir*, 1996, **12**, 2125.
73. S. Shibuichi, T. Onda, N. Satoh and K. Tsujii, *J. Phys. Chem.*, 1996, **100**, 19512.

74. K. Tadanaga, J. Morinaga, A. Matsuda and T. Minami, *Chem. Mater.*, 2000, **12**, 590.
75. K. Tadanaga, J. Morinaga and T. Minami, *J. Sol-Gel Sci. Technol.*, 2000, **19**, 211.
76. A. Fujishima, T. N. Rao and D. A. Tryk, *Electrochim. Acta*, 2000, **45**, 4683.
77. A. Hattori, T. Kawahara, T. Uemoto, F. Suzuki, H. Tada and S. Ito, *J. Colloid Interface Sci.*, 2000, **232**, 410.
78. W. Barthlott and C. Neinhuis, *Planta*, 1997, **202**, 1.
79. R. Wang, K. Hashimoto, A. Fujishima, M. Chikuni, E. Kojima, A. Kitamura, M. Shimohigoshi and T. Watanabe, *Nature*, 1997, **388**, 431.
80. L. Zhang, R. Dillert, D. Bahnemann and M. Vormoor, *Energy Environ. Sci.*, 2012, **5**, 7491.
81. R. N. Wenzel, *Ind. Eng. Chem.*, 1936, **28**, 988.
82. S. Permpoon, M. Houmard, D. Riassetto, L. Rapenne, G. Berthome, B. Baroux, J. C. Joud and M. Langlet, *Thin Solid Films*, 2008, **516**, 957.
83. A. I. Kontos, A. G. Kontos, D. S. Tsoukleris, G. D. Vlachos and P. Falaras, *Thin Solid Films*, 2007, **515**, 7370.
84. S. Song, L. Q. Jing, S. D. Li, H. G. Fu and Y. B. Luan, *Mater. Lett.*, 2008, **62**, 3503.
85. A. A. Ashkarran and M. R. Mohammadizadeh, *Mater. Res. Bull.*, 2008, **43**,

522.

86. H. Kim, S. J. Jung, Y. H. Han, H. Y. Lee, J. N. Kim, D. S. Jang and J. J. Lee, *Thin Solid Films*, 2008, **516**, 3530.
87. B. Leclercq, M. Sotton, A. Baszkin and L. Terminassiansaraga, *Polymer*, 1977, **18**, 675.
88. B. Gupta, J. Hilborn, C. Hollenstein, C. J. G. Plummer, R. Houriet and N. Xanthopoulos, *J. Appl. Polym. Sci.*, 2000, **78**, 1083–1091.
89. E. M. Liston, L. Martinu and M. R. Wertheimer, *J. Adhes. Sci. Technol.*, 1993, **7**, 1091.
90. L. Zhang, X. Y. Zhang, Z. Dai, J. J. Wu, N. Zhao and J. Xu, *J. Colloid Interface Sci.*, 2010, **345**, 116.
91. D. Lee, M. F. Rubner and R. E. Cohen, *Nano Lett.*, 2006, **6**, 2305.
92. L. Xu and J. He, *ACS Appl. Mater. Interfaces*, 2012, **4**, 3293.
93. L. Xu, J. He and L. Yao, *J. Mater. Chem. A*, 2014, **2**, 402.
94. X. Li and J. He, *ACS Appl. Mater. Interfaces*, 2012, **4**, 2204.
95. D. M. Sim, M. Choi, Y. H. Hur, B. Nam, G. Chae, J. H. Park, Y. S. Jung, *Adv. Optical Mater.*, 2013, **1**, 428.
96. P. Patel, C. K. Choi and D. D. Meng, *J. Assoc. Lab. Autom.*, 2010, **15**, 114.
97. J. M. Corres, I. R. Matias, M. Hernaez, J. Bravo, F. J. Arregui, *IEEE Sensors Journal*, 2008, **8**, 281.

98. D. Tahk, T. Kim, H. Yoon, M. Choi, K. Shin and K. Y. Suh, *Langmuir*, 2010, **26**, 2240.

Chapter II.

Photosensitive double-layered anti-reflection film containing a europium(III) complex

II-1. Introduction

In recent years, as their sizes have increased, flat panel displays have attracted considerable interest for use in the delivery of presentations. Direct presentation on a flat panel display screen can provide bright and clear images with a higher contrast ratio than images using the beam projection system composed of a beam projector and a white screen. However, the problem with flat panel displays is that it is difficult to optically highlight specific content on the screen using a laser pointer or laser pen. The anti-reflection coating^[1-6] applied on the top of the display screen diminishes the reflection of the laser light. Furthermore, the display is self-lightening and the bright light from the backlight of the display interrupts the detection of the laser light.^[7] Several researches have been conducted on luminescent anti-reflection films that contain metal oxides in order to overcome this problem.^[8-11] However, obstacles to the practical application of these films remain, such as the high temperature process required for the fabrication of the coating layer and the difficulty in selecting an excitation wavelength outside of the backlight spectrum of the display. Photochromic materials have also been considered, but cannot be used because of their slow response and low fatigue resistance.^[12]

In this work, laser visibility on a double-layered anti-reflection film with a

high refractive index layer containing a photoluminescent europium(III) complex was demonstrated. The europium(III) ion shows a narrow emission and long life because its luminescence is derived from intraconfigurational f-f transitions. Direct irradiation of the europium(III) ion is difficult due to its low absorption coefficient. Therefore, the europium(III) ion is used for practical applications after complexation with organic molecules which absorb light and sensitize the ion by intramolecular energy transfer.^[13,14] The absorption pattern of the complex can be controlled easily by varying the organic ligand structures. In addition, the europium(III) complex shows a relatively large Stokes shift between absorption and emission. By considering these advantages, the europium(III) complex can be excited at near-UV wavelengths, which are rarely emitted by the display, and the photoluminescence of the europium(III) complex can be detected in the visible range.

II-2. Experimental

Materials. Tris(1,3-diphenyl-1,3-propanedionato)(1,10-phenanthroline) europium(III) (TDPP-Eu(III)) was purchased from TCI and was used without further purification. Dipentaerythritol hexaacrylate (Miramer M600) was purchased from Miwon Specialty Chemical. 1-Hydroxycyclohexyl phenyl ketone was purchased from Aldrich. Colloidal nano-silica sol (IPA-ST-MS, solid contents 20 wt%) was purchased from Nissan Chemical. Other solvents were used as received.

Preparation of an europium(III) complex containing high refractive index coating solution (HR-Eu). A UV curable acrylate solution was prepared by dissolving Miramer M600 (0.16 g, 25.37mM), 1-hydroxycyclohexyl phenyl ketone (0.01 g, 6.25 mM), and TDPP-Eu(III) (0.08 g, 6.84 mM) in THF (10.97 ml). The total solid contents was 2.5 wt%.

Preparation of a low refractive index coating solution (LR-silica). A colloidal nano-silica solution was prepared by diluting 0.1 g of IPA-ST-MS in 9.9 g (12.60 mL) of isopropyl alcohol and stirred for 10 min at room temperature. The total solid contents was 2 wt%.

Preparation of europium(III) complex containing anti-reflection film (AR-Eu). HR-Eu (200 μL) was dropped on the glass substrate ($5 \times 5 \text{ cm}^2$), followed by spin coating at 400 rpm for 30 sec. The coated glass was cured by a 100W high pressure mercury lamp under nitrogen. Total irradiation dose was 400 mJ cm^{-2} . Then, LR-silica (200 μL) was applied on the top of the high refractive index layer by spin coating at 1000 rpm for 30 sec.

Instrument. UV-Vis absorption spectrum was obtained by a Sinco S-3150 spectrometer. Fluorescence measurements were performed on a Shimadzu RF-5301PC spectrofluorometer. Refractive indices and reflectance were measured by a K-Mac ST4000-DLX reflectometer. Transmitted white LED backlight spectrum of LCD was investigated by a Topcon SR-UL1R spectroradiometer. Cross-sectional layer analysis was performed by a Hitachi S-4300 FE-SEM. A Philips TL 100W/10R lamp (wavelength; between 350 and 400 nm) was used for irradiation of a TDPP-Eu(III)-containing layer.

Photoluminescent pointing test. A surface-protective-coated polarizer film of an LCD (Samsung smart TV model UN32ES6400) was replaced by an uncoated glare polarizer film. The AR-Eu coated glass or uncoated glass was attached on the glare polarizer film and the pointing test was carried out using a

405 nm laser pointer.

II-3. Results and discussion

Anti-reflection is achieved by the destructive interference between two types of reflected light originated from the surface of the coating layer and the interface between the coating layer and the substrate. To successfully achieve anti-reflection, it is essential to match the two conditions. Firstly, the phase difference between the two types of reflected light should be half of the wavelength. Secondly, the intensities of the two types of reflected light should be equal.^[1,15] Both conditions can be expressed as equation I-2 and I-3, respectively, as follows:

$$n_c^2 = n_s \quad (\text{Equation I-2})$$

$$2 n_c d_c = \lambda/2 \quad (\text{Equation I-3})$$

where n_c , n_s refer to the refractive indices of the coating layer, substrate, respectively, d_c is the thickness of the coating layer and λ is the wavelength of the light.

The refractive index of the coating layer should be 1.22 to prevent light reflection from the glass substrate (refractive index of 1.5) according to equation I-2. Although some low refractive index materials are available such

as silica (refractive index of 1.46) and magnesium fluoride (refractive index of 1.39), they do not achieve perfect anti-reflection. Due to the difficulty of attaining a low refractive index near 1.22, an anti-reflection film generally has a multi-layered structure. The equations for a double-layered anti-reflection coating are as follows:

$$(n_s / n_{\text{air}}) n_1^2 = n_2^2 \quad (\text{Equation I-6})$$

$$n_1 d_1 = n_2 d_2 = \lambda/4 \quad (\text{Equation I-7})$$

where n_1 and d_1 are the refractive index and thickness of the upper layer, respectively, and n_2 and d_2 are those of the bottom layer. n_s is the refractive index of the substrate and n_{air} is the refractive index of air.

In a double-layered anti-reflection system with the bottom layer of a high refractive index and the upper layer of a low refractive index, equation I-7 suggests that the refractive index of the upper layer is not necessarily as low as 1.22 when the refractive index of the bottom layer is high.

Tris(1,3-diphenyl-1,3-propanedionato)(1,10-phenanthroline)europium(III) (TDPP-Eu(III)) was choosed as a photosensitive compound for highlighting because the absorption spectrum of TDPP-Eu(III) was out of the backlight

spectrum of the LCD and could be excited to emit red light by using a commercially available laser source. In addition, TDPP-Eu(III) was soluble in various organic solvents and commercially available. A UV cured acrylate film containing TDPP-Eu(III) and a film of a colloidal nano-silica were used as a high and a low refractive index layer, respectively, for the fabrication of an anti-reflection film. Figure II-1 shows the absorption, excitation, and emission spectra of TDPP-Eu (III) in THF and the transmitted white LED backlight spectrum of the LCD. When irradiated by near-UV such as the 405 nm laser light, TDPP-Eu (III) showed a strong red emission at 615 nm, corresponding to the $^5D_0 \rightarrow ^7F_2$ transition of the Eu (III) ion. Emission peaks at 581 nm, 594 nm, and 654 nm were assigned to the $^5D_0 \rightarrow ^7F_0$, $^5D_0 \rightarrow ^7F_1$, and $^5D_0 \rightarrow ^7F_3$ transitions, respectively. The absorption and excitation spectra of TDPP-Eu (III) barely overlapped with the transmitted white LED backlight spectrum of the LCD, indicating that TDPP-Eu(III) in the anti-reflection film would not disturb the display images when the film was placed on the top of the display screen. It was also expected that the illumination on the anti-reflection film containing TDPP-Eu(III) by a laser beam of appropriate wavelength could be possible even in the presence of a backlight.

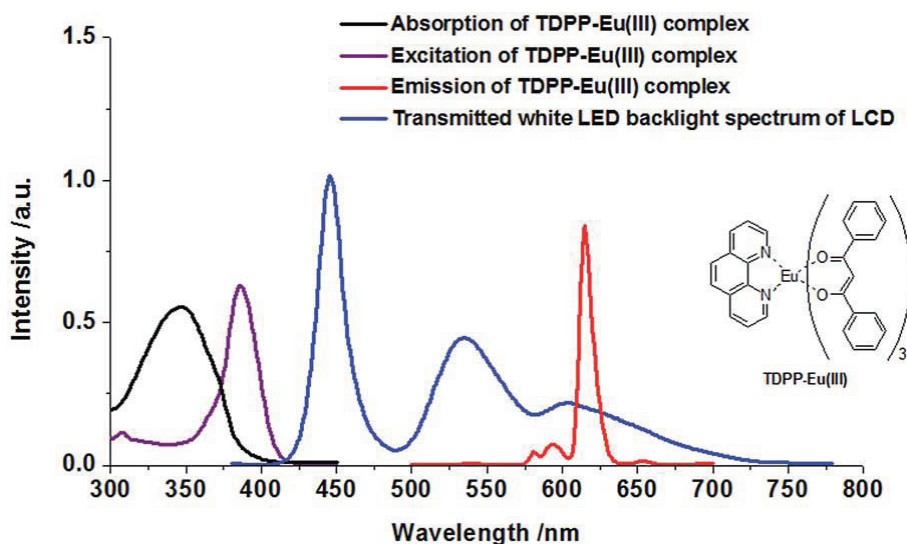


Figure II-1. Normalized absorption, excitation ($\lambda_{\text{em}} = 615 \text{ nm}$) and emission ($\lambda_{\text{ex}} = 405 \text{ nm}$) spectra of TDPP-Eu(III) in THF (10^{-2} mM) and transmitted white LED backlight spectrum of the LCD.

A UV curable acrylate solution containing TDPP-Eu(III) in THF (HR-Eu) was prepared from TDPP-Eu(III) (6.84 mM), a dipentaerythritol hexaacrylate (Miramer M600) (25.37 mM) and 1-hydroxycyclohexyl phenyl ketone (6.25 mM). A clear thin film containing TDPP-Eu(III) was obtained by spin coating of the solution on the glass substrate and subsequent UV curing. The HR-Eu coated glass emitted bright red light, whereas the uncoated glass was photophysically silent under the near-UV irradiation with a Philips TL 100W/10R lamp (spectral range from 350 to 400 nm) as shown in Figure II-2.

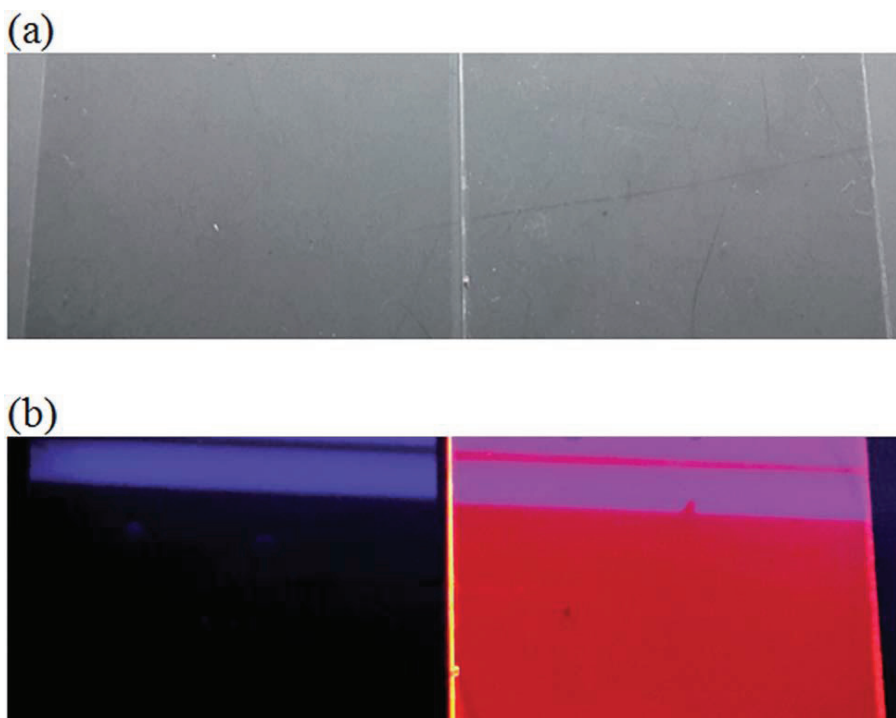


Figure II-2. Photographs of the uncoated glass (left) and the TDPP-Eu(III) coated glass (right) under visible light (a) and under near-UV light (b).

The concentration effects of TDPP-Eu (III) on the refractive index of the acrylate film were examined. The films with different TDPP-Eu (III) compositions were prepared on a glass substrate by spin coating of the acrylate solutions containing various concentrations of TDPP-Eu (III) in THF. The thicknesses of the films were set to be over 100 nm in order to measure the refractive indices correctly. For the measurement, green 555 nm light was used, which is known to be the most sensitive to human eyes.^[16] Figure II-3 shows

the refractive indices of the films depending on the compositions of TDPP-Eu(III). The refractive index of the acrylate film was 1.53 in the absence of TDPP-Eu(III) and increased proportionally as the composition of the Eu(III) complex increased. The refractive index of TDPP-Eu(III) itself was 1.69.

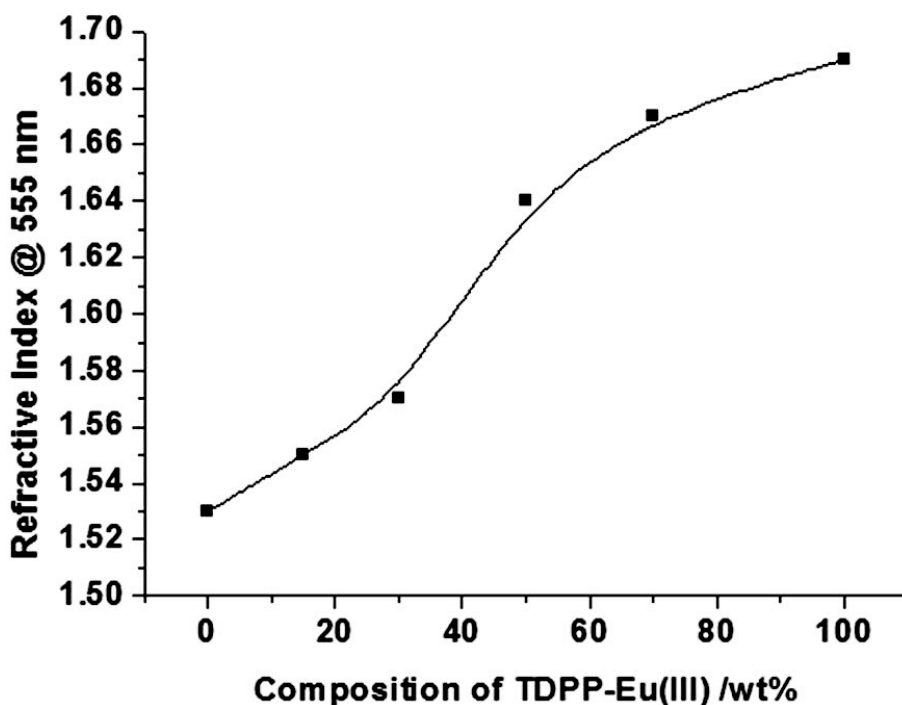


Figure II-3. Refractive indices of the films depending on TDPP-Eu(III) compositions.

To confirm the stability of the acrylate film having TDPP-Eu(III) at the display system, the UV stability of the TDPP-Eu(III) was investigated. Two

polarizer films were attached in parallel to the rear side of the Eu(III) complex coated glass. UV irradiation was carried out from the rear side with a high pressure mercury lamp and PL intensity was measured every 3,000 mJ/cm² up to 9,000 mJ/cm². The emission intensity was slightly decreased after UV irradiation of 9,000 mJ/cm² (Figure II-4).

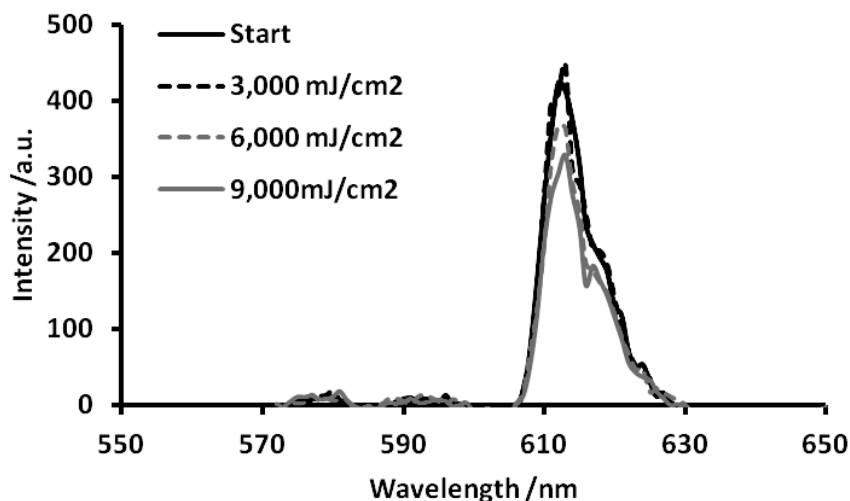


Figure II-4. The emission of the Eu(III) complex ($\lambda_{ex} = 405$ nm) coated glass before and after UV irradiation.

As a low refractive index layer, a thin film was prepared from a colloidal nano-silica sol (LR-silica).^[17] The film showed a refractive index of 1.34, which was much lower than the intrinsic refractive index of silica (1.46). Randomly

packed spherical particles without interparticle forces have been reported to have void fractions ranging from 37 % to 42 % in their packing structures.^[18,19] Because of the interparticle voids, the colloidal nano-silica coated layer showed a relatively low refractive index. The calculated void fraction from the measured refractive index was about 26 %. It was presumed that the porosity lower than the reported values resulted from the irregularity of the silica particles (Figure II-5).^[20,21]

A double-layered anti-reflection film (AR-Eu) was prepared from HR-Eu and LR-silica. HR-Eu was first coated on the glass substrate and cured to give a high refractive index layer [composition of TDPP-Eu(III): 30 wt%]. A LR-silica layer of a low refractive index was then applied on the top of the high refractive index layer. The refractive index of the HR-Eu layer in AR-Eu was measured to be 1.57. The refractive index of the LR-silica layer slightly increased from 1.34 for the single LR-silica layer to 1.37, which probably resulted from the porosity change. According to equation I-7, when the refractive index of the top layer was 1.37, the bottom layer should have a refractive index of 1.68 to achieve a perfect anti-reflective effect. This value could be achieved using a solution of a high concentration of TDPP-Eu (III), but the film with a TDPP-Eu (III) composition of over 30 wt% showed poor quality due to nonhomogeneous

crosslinking.

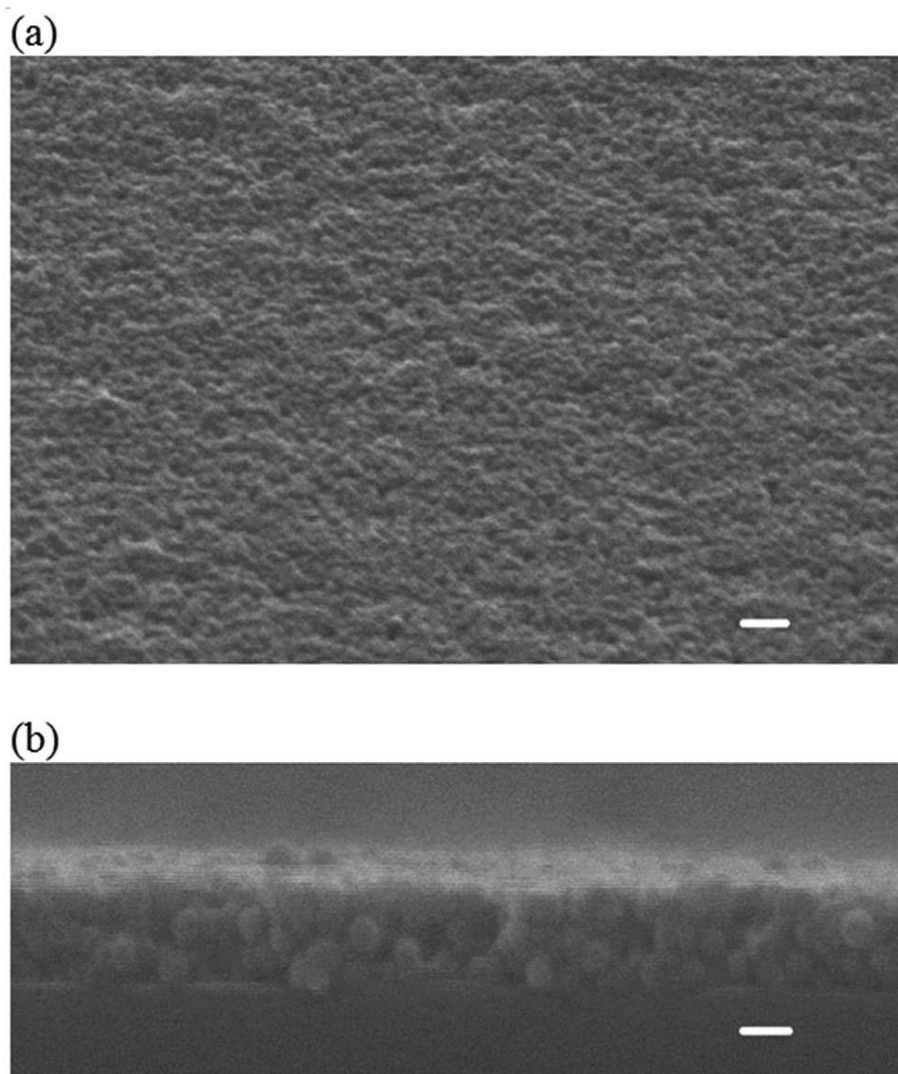


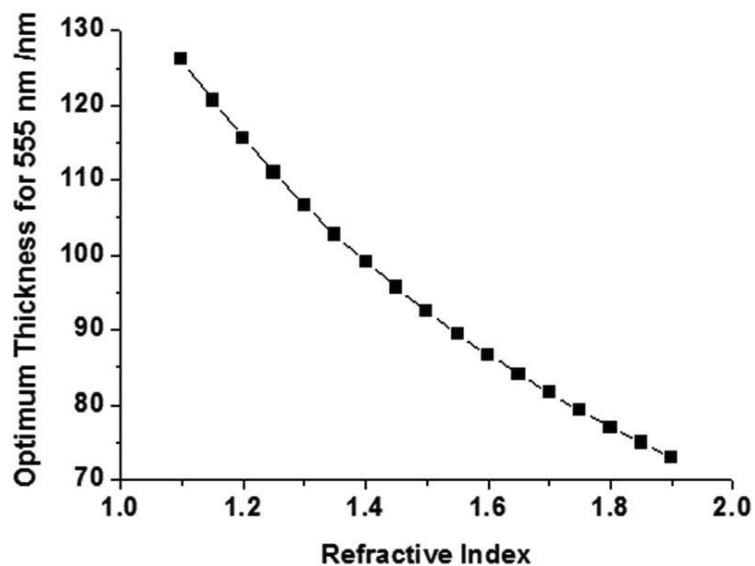
Figure II-5. SEM images of (a) the surface and (b) the cross-section of the **LR-silica** layer. Scale bar is 100 nm for (a) and 50 nm for (b).

According to equation I-7, the theoretically optimized thicknesses of the high and low refractive index layers for visible light at 555 nm were 88 and 101 nm, respectively, when their refractive indices were 1.57 and 1.37, respectively (Figure II-6a).

The spin coating rate for each layer was controlled to have an optimum thickness. Figure II-6b shows the SEM image of the cross-section of AR-Eu. The thickness of the bottom layer was measured to be around 85 nm (HR-Eu layer) and that of the upper layer was around 100 nm (LR-silica layer), and these were very close to the optimum thicknesses. The AR-Eu film eventually showed the minimum reflectance at 551 nm.

The uncoated glass showed a reflectance of around 4 % at 555 nm (Figure II-7). The reflectance of the HR-Eu coated glass was increased to 6 % because of its enhanced reflection at the surface and at the interface of the coating layer and the substrate. The reflectance of the LR-silica coated glass was 0.81 %. The reflectance of AR-Eu composed of the HR-Eu and LR-silica layers was dramatically reduced to 0.48 % at 555 nm. The reflectance spectrum of each sample measured between 400 ~ 700 nm was very similar to the calculated spectrum based on Fresnel's equation.^[1]

(a)



(b)

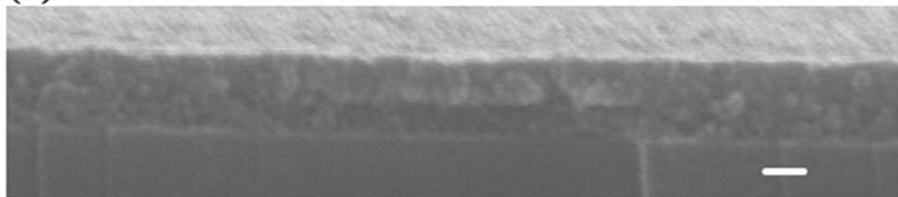


Figure II-6. (a) Calculated optimum thickness as a function of a refractive index. (b) Cross-sectional SEM image of the **AR-Eu** layer on the glass. Scale bar is 100 nm.

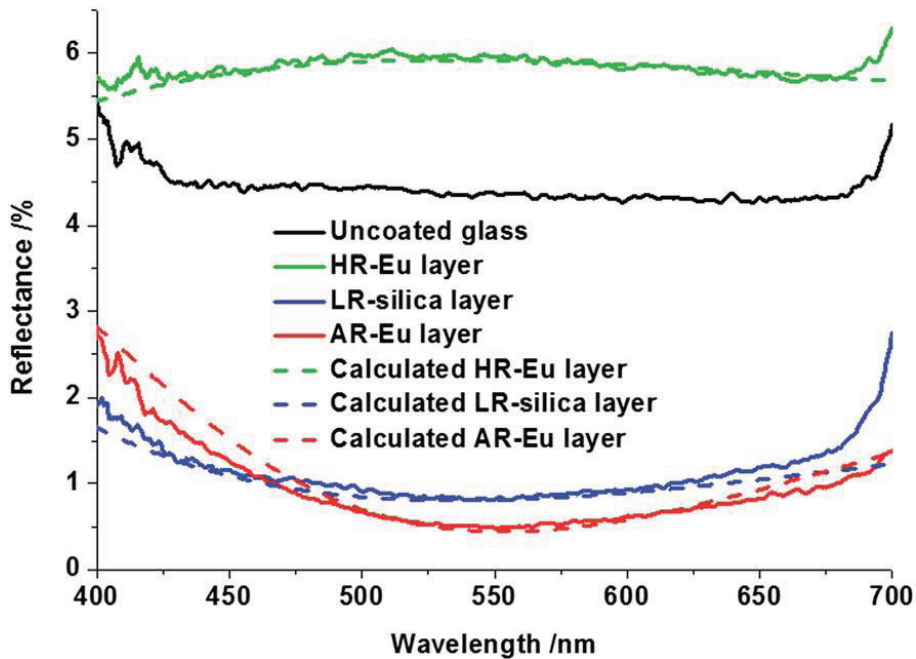


Figure II-7. Reflectance of the uncoated glass and the surface-coated glass. The calculated reflection spectra of the HR-Eu and LR-silica films on the glass were obtained considering their refractive indices of 1.57 and 1.34, respectively, and thicknesses of 85 and 100 nm, respectively. The calculated reflection spectrum of the AR-Eu film on the glass was obtained based on the bottom layer, with a refractive index of 1.57 and a thickness of 88 nm, and on the top layer with a refractive index of 1.37 and a thickness of 101 nm.

An AR-Eu coated glass substrate was placed on the top of the glare polarizer of the LCD, on which letters were displayed. A photograph of the display taken under irradiation using an indoor fluorescent lamp showed that the letters were

clearly visible (Figure II-8). An uncoated glass substrate was similarly placed on the LCD; in this case, the fluorescent lamp reflected strong light, making it difficult to recognize some of the letters on the display. It was also possible to highlight a specific point on the AR-Eu coated display screen using the laser light. When a 405 nm laser pointer was used, the pointed area appeared as a bright red spot because the europium (III) complex in the AR-Eu layer was excited by the laser light (Figure II-9). In contrast, the area highlighted by the laser-pointer was barely recognizable on the uncoated screen due to the bright backlight of the display.

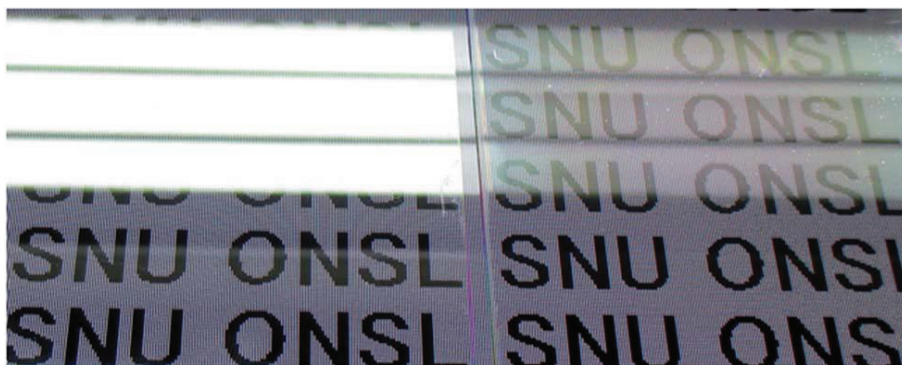


Figure II-8. Photographs of the uncoated display screen (left) and the **AR-Eu** coated display screen (right) under irradiation by an indoor fluorescent lamp.

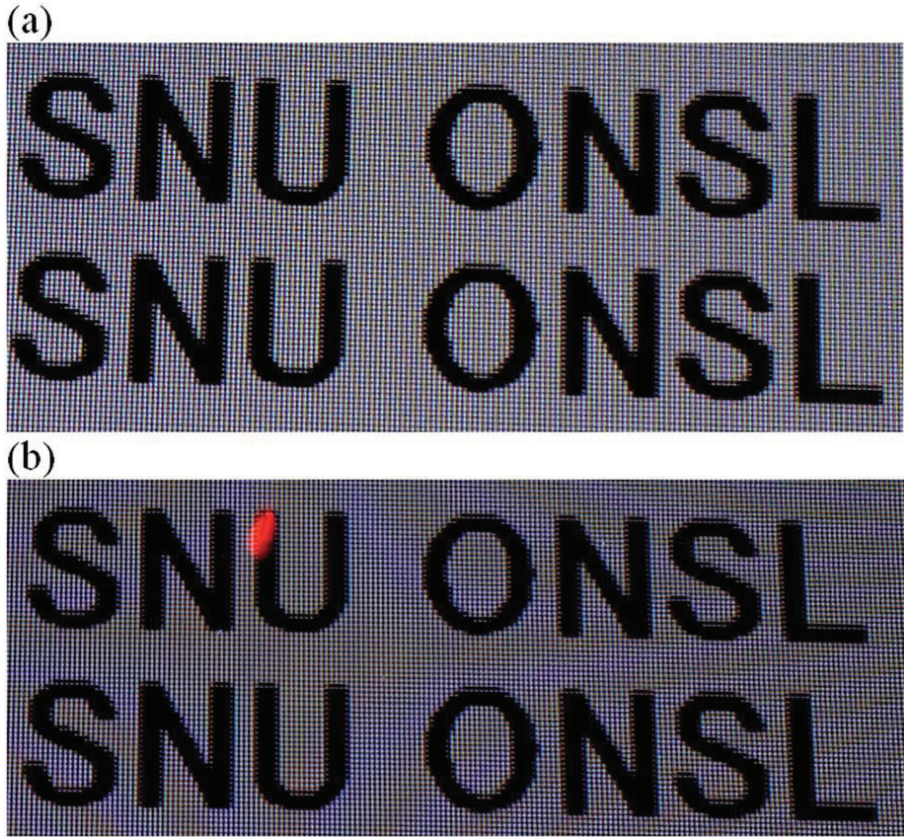


Figure II-9. Photographs of the uncoated display screen (a) and the **AR-Eu** coated display screen (b) taken while using a 405 nm laser pointer.

II-4. Conclusions

A double-layered anti-reflection film with a high refractive index layer containing an europium (III) complex was prepared. The europium (III) complex acted as a high refractive index material as well as a photosensitive material. When the anti-reflection film was placed on the top of the glare polarizer of the LCD, It was possible to selectively highlight a displayed image using near-UV laser light and to simultaneously eliminate unnecessary reflection of outside light. These anti-reflection and photosensitive coatings could be used in various devices such as displays, sensors for communication systems, solar cells, and functional windows.

II-5. References

1. H. K. Raut, V. A. Ganesh, A. S. Nair and S. Ramakrishna, *Energy Environ. Sci.*, 2011, **4**, 3779.
2. M. Ibn-Elhaj and M. Schadt, *Nature*, 2001, **410**, 796.
3. Y. Du, L. E. Luna, W. S. Tan, M. F. Rubner and R. E. Cohen, *ACS Nano*, 2010, **4**, 4308.
4. S. Kim, J. Cho and K. Char, *Langmuir*, 2007, **23**, 6737.
5. M. Yamaguchi, H. Nakayama, K. Yamada and H. Imai, *Optics Letters*, 2009, **34**, 2060.
6. T. Taguchi, H. Hayashi, A. Fujii, K. Tsuda, N. Yamada, K. Minoura, A. Isurugi, I. Ihara and Y. Itoh, *SID Symposium Digest*, 2010, **41**, 1196.
7. K. Takada, *US Pat.*, 20090231713A1, 2009.
8. B. Lee, E. Lee and S. Byeon, *Adv. Funct. Mater.*, 2012, **22**, 3562.
9. N. Watanabe and S. Fujihara, *Ind. Eng. Chem. Res.*, 2011, **50**, 5611.
10. S. Tanaka and S. Fujihara, *Int. J. Appl. Ceram. Technol.*, 2011, **8**, 1001.
11. S. Tanaka and S. Fujihara, *Langmuir*, 2011, **27**, 2929.
12. G. Such, R. A. Evans, L. H. Yee and T. P. Davis, *J. Macromol. Sci. Polymer. Rev.*, 2003, **43**, 547.
13. S. I. Weissman, *J. Chem. Phys.*, 1942, **10**, 214.

14. K. Binnemans, *Chem. Rev.*, 2009, **109**, 4283.
15. H. A. Macleod, in *Thin-film Optical Filters*, McGraw Hill, USA, 1989.
16. H. Gross, F. Blechinger, B. Achtner, in *Handbook of optical systems*, Wiley-VCH, Germany, 2008.
17. B. G. Prevo, Y. Hwang and O. D. Velev, *Chem. Mater.*, 2005, **17**, 3642.
18. A. J. Forsyth, S. R. Hutton, C. F. Osborne and M. J. Rhodes, *Phys. Rev. Lett.*, 2001, **87**, 244301-1.
19. D. J. Cumberland and R. J. Crawford, in *Packing of Particles*, Elsevier Science, Netherlands, 1987.
20. K. T. Cook, K. E. Tettery, R. M. Bunch, D. Lee and A. J. Nolte, *ACS Appl. Mater. Interfaces*, 2012, **4**, 6426.
21. A. Donev, I. Cisse, D. Sachs, E. A. Variano, F. H. Stillinger, R. Connelly, S. Torquato and P. M. Chaikin, *Science*, 2004, **303**, 990.

Chapter III.

**Anti-reflective film prepared by the surface assembled
of hollow silica nanoparticles**

III-1. Introduction

For anti-reflection coating of polymer substrates, functionally separate multiple layers are usually needed. A hard coating layer for protecting the film is first coated on a polymer substrate, following which high and low refractive index layers are coated on the hard coating layer. To achieve the destructive interference of the reflected light, it is necessary to control the coating thickness of the low refractive index layer to be in the range of nanometers. For accurately controlling the layer's thickness, stepwise layer-by-layer assembly and dip coating methods have been widely investigated^[1-8] but, it is still a challenge to efficiently fabricate anti-reflection films. Recently, the need for a simple and convenient process for enhancing the production efficiency of the films has grown.

We report a simple anti-reflection coating method of polymer substrates using aggregation behaviors of hollow silica nanoparticles. The aggregation behaviors of hollow silica nanoparticles and the solvent swelling effects of the polymer substrates on the optical properties are discussed in comparison with the results from a glass substrate. Surface localization of nanomaterials has been widely investigated in many fields but been rarely studied to achieve

antireflection properties.^[9,10] and are compared with those for a glass substrate.

III-2. Experimental

Materials. Hollow silica nanoparticles, dispersed in methyl isobutyl ketone (Thruhya4120, solid content of 20 wt%), were purchased from JGC&C. Pentaerythritol triacrylate (Miramer M340) was purchased from Miwon Specialty Chemical. 1-Hydroxycyclohexyl phenyl ketone was purchased from Aldrich. Other solvents were used as received.

Preparation of a UV curable acrylate solution. A UV curable acrylate solution was prepared by dissolving Miramer M340 (3.00 g, 1.35 mM) and 1-hydroxycyclohexyl phenyl ketone (0.30 g, 0.20 mM) in 6.70 g (7.43 mL, 76.04 mmol) of ethyl acetate. The total solid content was 33 wt%.

Preparation of a UV curable hollow silica coating solution (HS-AR-15~HS-AR-70). All the coating solutions in this study were prepared by simply mixing the dispersed hollow silica nanoparticles with a UV curable acrylate solution and an additional solvent, at various ratios. The ratios of the hollow silica nanoparticles to the total solid content were 15 wt% (HS-AR-15), 20 wt% (HS-AR-20), 30 wt% (HS-AR-30), 40 wt% (HS-AR-40), 50 wt% (HS-AR-50), 60 wt% (HS-AR-60), and 70 wt% (HS-AR-70), respectively. For all coating

solutions the total solid content was maintained at 4.76 wt%, and the solvent ratio was also maintained at 50 (EA) : 50 (MIBK) wt%.

Preparation of anti-reflection films. In each experiment, 1 g of the prepared coating solution was loaded on a triacetyl cellulose film (TAC; thickness, 40 μm) and coated by a wire bar #7. The wet film's thickness was 16 μm . The coated wet films were dried at 90 $^{\circ}\text{C}$ for 2 min to remove the solvent by evaporation. Finally, the dried films were UV-cured by a 100 W high-pressure mercury lamp in the presence of gaseous nitrogen. The overall irradiation dose was 400 mJ/cm^2 .

Instrument. Reflectance was measured using a Shimadzu UV-2450 device. Refractive indices were measured using a K-Mac ST4000-DLX reflectometer. Scanning electron microscopy (SEM) images were obtained using a Hitachi S-4300 FE-SEM. Energy-dispersive X-ray spectroscopy (EDS) analysis was performed using a Thermo NORAN System SIX. Transmission electron microscopy (TEM) images were obtained using a JEOL JEM-2010 microscope at 200 keV. Pencil hardness was measured using a Sukbo Science ED-PC2 pencil hardness tester.

III-3. Results and discussion

Hollow silica nanoparticles have been investigated as low refractive index materials owing to their highly porous structures. These particles have thin shells and large pores in their core, which effectively reduces their refractive index. To fabricate anti-reflection films, the morphology and the refractive indices of hollow silica nanoparticles were investigated first. TEM analysis was performed to characterize hollow silica nanoparticles (Figure III-1). The particles' diameter was in the 40–80 nm range, and the shell thickness ranged from 5 nm to 10 nm. The refractive index of hollow silica nanoparticles was measured and compared to the refractive index calculated based on the particles' core-shell volume fraction.

The dispersion containing hollow silica nanoparticles (ThruIya4120) was spin-coated on a silicon wafer and the refractive index of the resulting coating layer was analyzed in the visible range (Figure III-2). Although the measured refractive index of the coating layer was 1.19 at 555 nm, the real refractive index of hollow silica nanoparticles was estimated as 1.27, assuming the inter-particle pore volume in the packing layer is 30%, which reduces the refractive index even more.

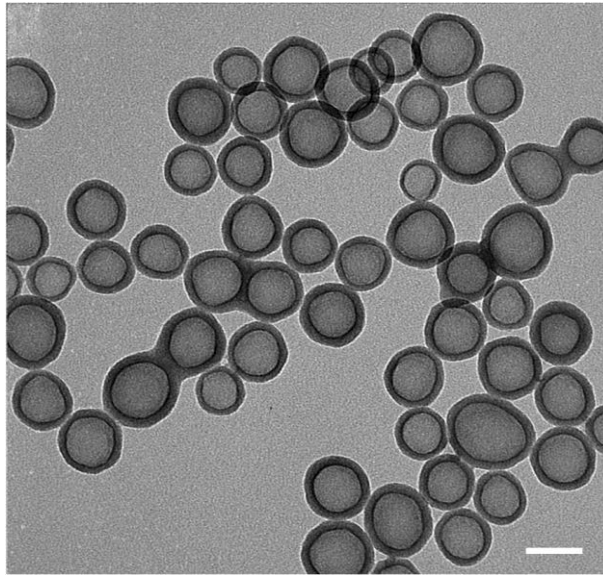


Figure III-1. TEM imaging of hollow silica nanoparticles. The scale bar is 50 nm.

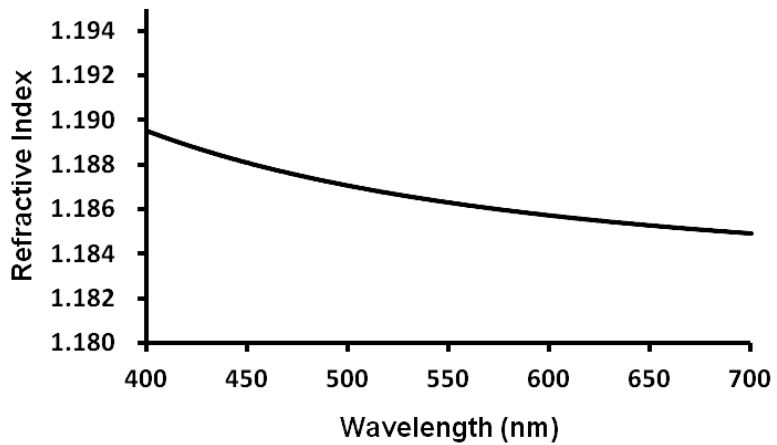


Figure III-2. Refractive index of a layer of hollow silica nanoparticles, with inter-particle pores.

The refractive index of hollow silica nanoparticles was calculated from the TEM imaging data and compared to the measured refractive index. As the measured hollow silica nanoparticles exhibited a relatively broad range of diameters and shell thicknesses, the refractive index of hollow silica nanoparticles was calculated depending on these two parameters. The shell thickness varied from 5 nm to 10 nm and the external diameter varied from 30 nm to 100 nm; the refractive indices of silica and air were set to 1.46 and 1.00, respectively (Figure III-3).

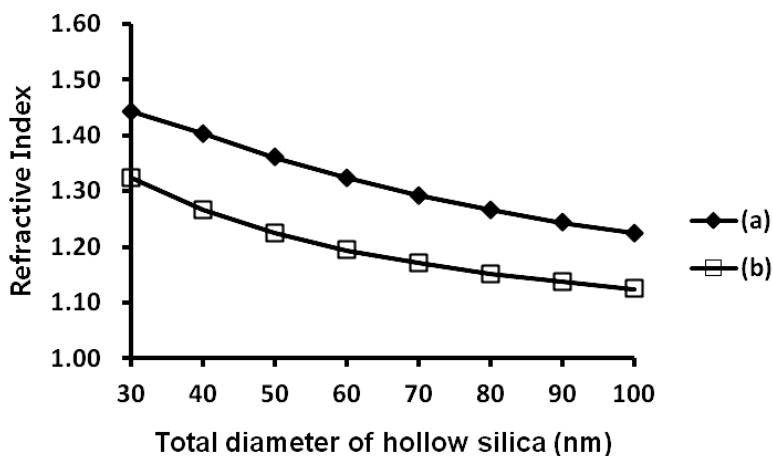


Figure III-3. Refractive indices of hollow silica nanoparticles, calculated from the particles' core-shell volume fraction. The shell thicknesses are (a) 10 nm and (b) 5 nm.

TEM imaging results reveal that smaller particles have thinner shells. For instance, the shell thickness of a typical 40-nm-diameter hollow nanoparticle is 5 nm, and that of a typical 80-nm-diameter particle is 10 nm. For both of particles, the refractive index is ~ 1.27 , because the core-shell volume fraction is nearly the same. This value matches the one obtained from direct measurements of the refractive index of a layer of hollow silica particles.

The dispersion of hollow silica particles and a UV curable acrylate solution were mixed at various ratios, and the refractive indices of the resulting mixtures were measured (Figure III-4a).

To investigate the substrate dependence of the optical properties of a coating solution, several HS-AR solutions were coated on glass substrates and polymer substrates, and the reflectance values of the resulting structures were measured. The mixed solutions were coated on the glass substrates and polymer substrates using a wire bar, and dried for 2 min at 90 °C, following which the surfaces were UV-cured using a 100 W high-pressure mercury lamp in the presence of gaseous nitrogen. The overall irradiation dose was 400 mJ/cm². The refractive index and reflectance decreased with increasing the portion of hollow silica nanoparticles (Figure III-4).

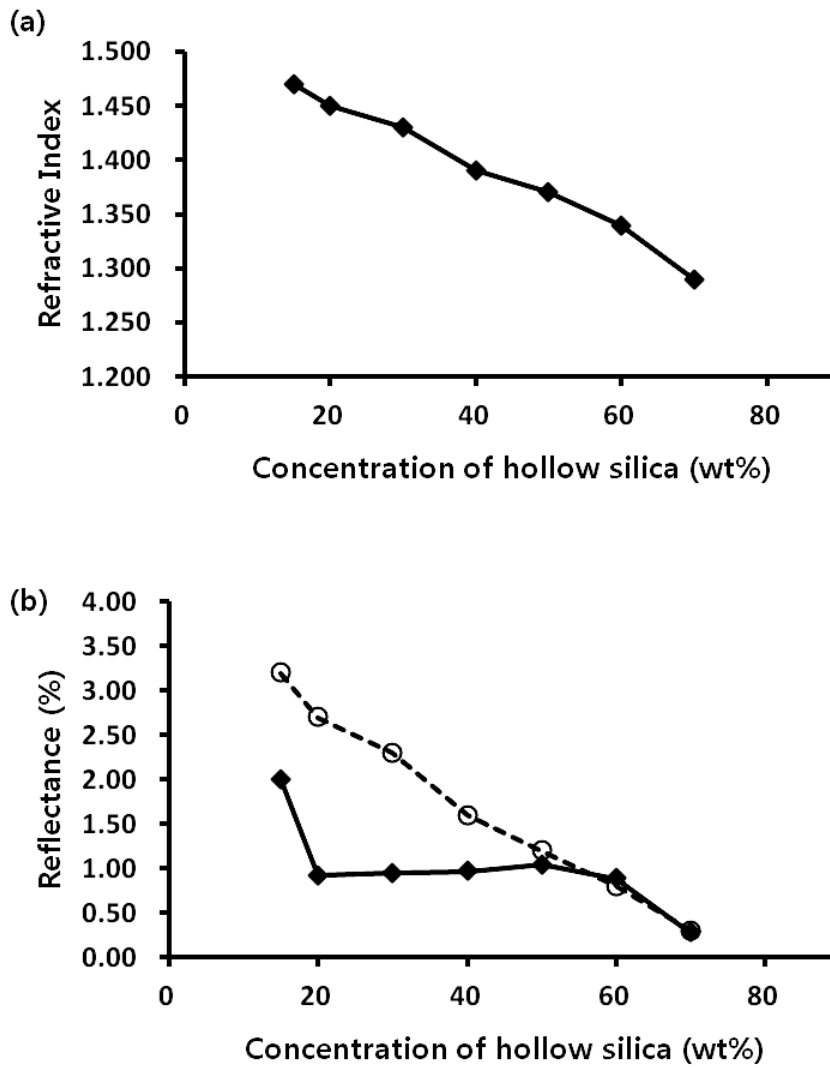


Figure III-4. (a) Refractive index and (b) reflectance of a coating layer, vs. the concentration of the hollow silica nanoparticles. The dashed line with circles: reflectance results for the glass substrate. The solid line with closed diamonds: reflectance results for the TAC substrate.

To reduce the reflectance below 1%, over 60 wt% of hollow silica nanoparticles is needed for the glass substrate, whereas only 20 wt% of hollow silica nanoparticles is needed for the polymer substrate. The dependence of reflectance on the concentration of hollow silica nanoparticles was quite different across the glass and polymer substrates. For the glass substrate, the reflectance matched the refractive index of the coating layer, depending on the concentration of hollow silica nanoparticles. On the other hand, for the polymer substrate the reflectance did not match the refractive index of the original coating solution. The reflectance was ~2% for the 15 wt% concentration of hollow silica nanoparticles (HS-AR-15), while it was 1% for concentrations ranging from 20 wt% (HS-AR-20) to 60 wt% (HS-AR-60), and it was 0.28% for 70 wt% (HS-AR-70).

To explain this dependence, morphological investigations were performed. 30 wt% of a solution of hollow silica nanoparticles (HS-AR-30) was coated on a glass and a TAC substrate using a wire bar over than 2- μ m-thickness, and the cross-sectional morphologies of the resulting films were investigated using SEM (Figure III-5).

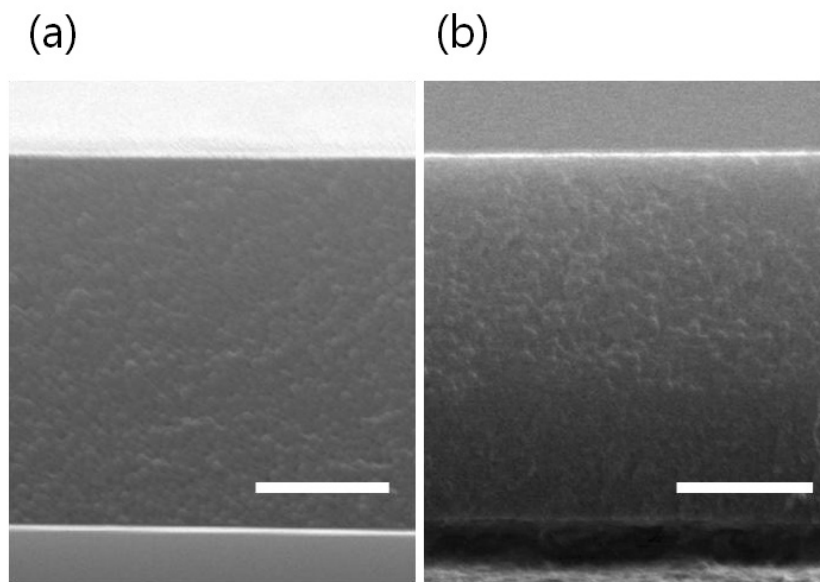


Figure III-5. Cross-sectional SEM images of a UV-curable solution of hollow silica nanoparticles (HS-AR-30) on the (a) glass substrate and (b) TAC substrate. The scale bar is 1 μm .

Based on the cross-sectional SEM images, the UV-curable coating of hollow silica nanoparticles on the glass substrate exhibited uniformly distributed hollow silica nanoparticles throughout the coating layer. However, for the UV-curable coating of hollow silica nanoparticles on the polymer substrate, the hollow silica nanoparticles accumulated closer to the upper surface of the coating layer and were rarely observed near the bottom surface of the coating layer. The distribution of hollow silica nanoparticles was confirmed by Si element profile analysis with EDS investigation (Figure III-6).

For the glass substrate, the Si element intensity only slightly increased from the upper surface to the bottom surface of the coating layer. However, for the polymer substrate the Si element intensity was dramatically lower on the bottom surface of the coating layer (compared with the upper surface), implying that in this case hollow silica nanoparticles in the coating layer were phase-separated in the vertical direction and were localized on the upper surface of the coating layer and rarely found on the bottom surface of the coating layer.

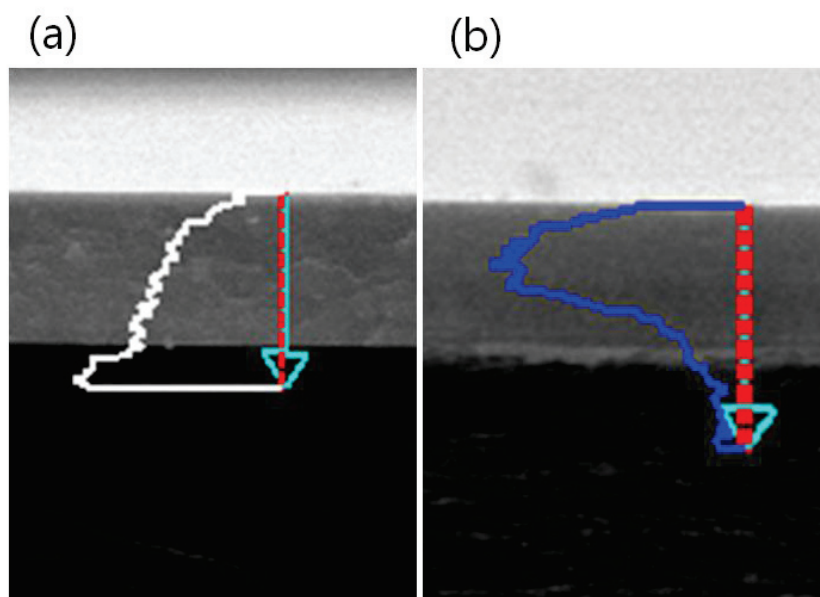


Figure III-6. Si profiles for solutions of UV-curable hollow silica nanoparticles on (a) the glass substrate and (b) the TAC substrate, obtained by the EDS analysis.

Owing to the above-described aggregation phenomenon, the optical properties of the coating on the polymer substrate differed from those of the coating on the glass substrate. To determine the refractive index of the layer of aggregated hollow silica nanoparticles coated on the polymer substrate, reflectance was calculated for the coating layers with different refractive indices coated on the TAC substrate with the refractive index of 1.47 (Figure III-7), and the result was compared to the measured reflectance.

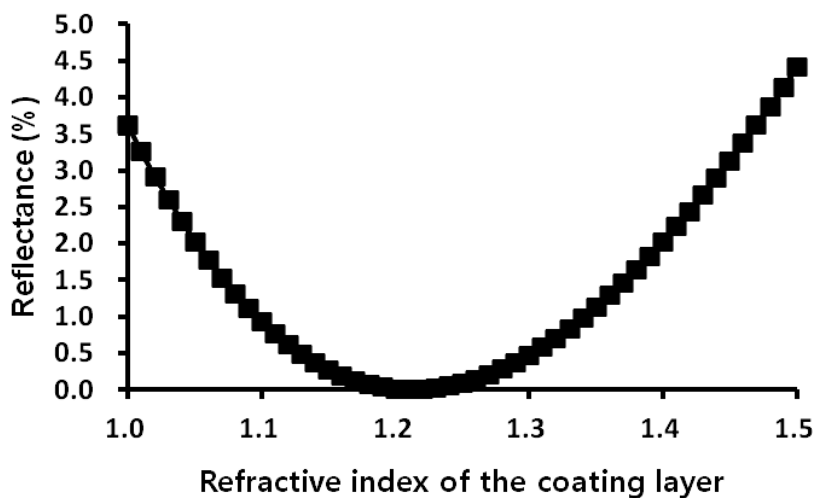


Figure III-7. Calculated reflectance vs. the refractive indices of the coating layer on the TAC film with the refractive index of 1.47.

The intrinsic refractive index of a layer coated with 15 wt% of hollow silica

nanoparticles solution (HS-AR-15) was 1.47. According to Figure III-7, the calculated reflectance of a TAC film coated with 15 wt% of hollow silica nanoparticles was 3.62%. However, the measured reflectance for this TAC substrate was 2%, and the calculated refractive index was 1.40.

To achieve the intrinsic refractive index of 1.40, ~40 wt% of hollow silica nanoparticles is needed. This implies that aggregation of hollow silica nanoparticles increases the concentration of hollow silica nanoparticles up to 2.7-fold for the upper top surface of the coating layer on the TAC substrate.

For the case of the TAC substrate, the aggregation behavior was observed for all solution ratios of hollow silica nanoparticles. However, the reflectance and the refractive index values remained nearly the same for nanoparticle solution concentrations ranging from 20 wt% (HS-AR-20) to 60 wt% (HS-AR-60).

To explain these phenomena, the refractive index of a fully concentrated layer of hollow silica nanoparticles with UV-curable acrylate was calculated. Assuming the inter-particle volume of 30% in the fully packed structure of nanoparticles, the refractive index of the fully packed layer of hollow silica nanoparticles with acrylate was 1.34 as calculated for a system for which 70% of the volume was taken up by hollow silica nanoparticles and 30% by UV-curable acrylate. From Figure III-7, the layer with the refractive index of 1.34

had the reflectance of ~1%.

These results suggest that for the 20 wt% solution concentration of hollow silica nanoparticles (HS-AR-20), the nanoparticles should be fully concentrated on the upper surface of the coating layer. From the same calculation, the coating layer with the 20 wt% solution concentration of hollow silica nanoparticles (HS-AR-20) yields a 3-fold more concentrated layer of hollow silica nanoparticles. The concentration of hollow silica nanoparticles was saturated and a fully packed structure was maintained for up to 60 wt% solution concentration of hollow silica nanoparticles (HS-AR-60). As a result, the reflectance remained at 1%.

Finally, a 70 wt% solution concentration of hollow silica nanoparticles (HS-AR-70), coated on the TAC substrate, yielded the reflectance as low as 0.28%, and the calculated refractive index was 1.28, which was the lower value than the fully saturated layer of hollow silica nanoparticles. In other words, for hollow silica nanoparticle concentrations above 70 wt%, the acrylate volume was not sufficient for filling the inter-particle pores, which reduced the refractive index and the reflectance of the coating layer dramatically.

To determine the mechanisms responsible for the observed surface aggregation behavior, coating solutions with various solvent ratios were coated by several micrometers thick on the TAC substrates, and the resulting morphologies were investigated (Figure III-8). In these characterizations, all of the chemical composition parameters except the solvent ratio were the same.

Because the swelling intensity of the TAC substrate obtained by EA is higher than that obtained by MIBK, the morphologies of the coating layer were investigated depending on the concentration of EA. As the concentration of EA decreased to 14 wt%, the extent of the substrate swelling decreased and the phase separation in the thickness direction decreased as well, compared with the 50 wt% of the EA solution (Figure III-8a, b). On the other hand, a very high concentration of the EA solution induced a strong swelling of the TAC substrate, making it difficult to distinguish the coating layer from the substrate (Figure III-8c). Even more, the swelled substrate component rose to the surface of the coating layer and increased the roughness of the coating surface, resulting in the diffusion of light.

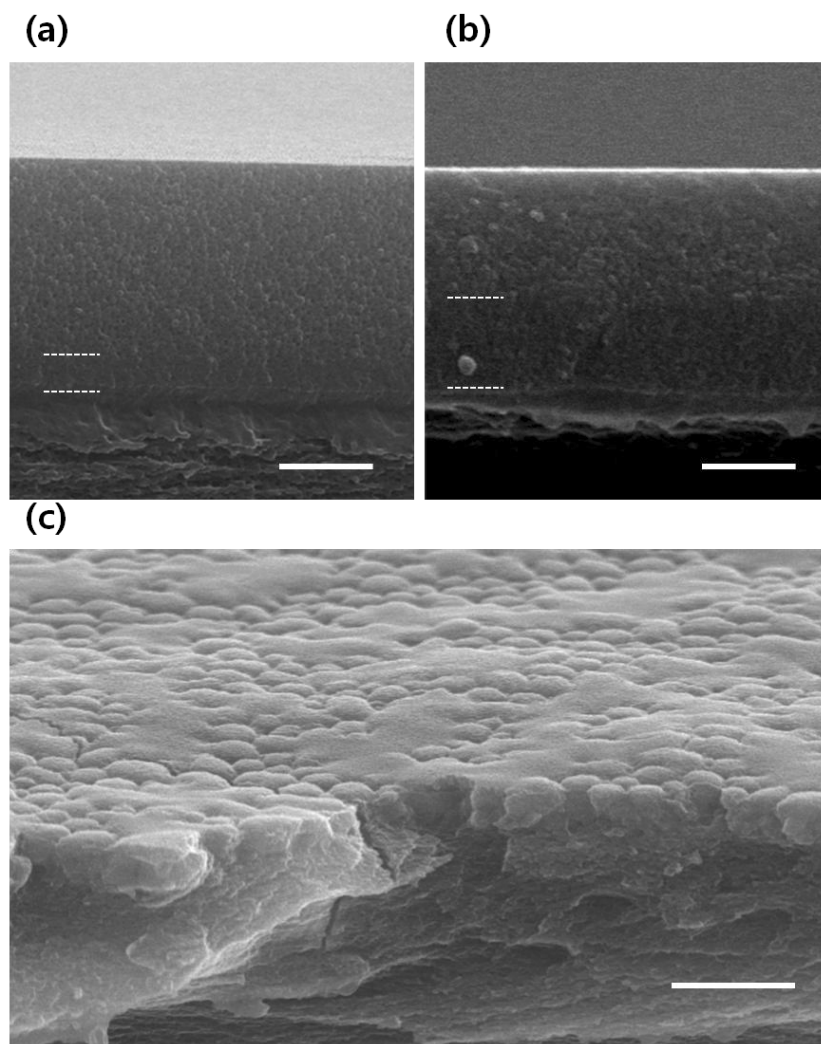


Figure III-8. Film SEM images for the solution with 30 wt% concentration of hollow silica nanoparticles coated on the TAC substrate: (a) for the EA to overall solvent ratio of 14 wt%, (b) for the EA to overall solvent ratio of 50 wt%, (c) for the EA to overall solvent ratio of 90 wt%. The scale bars in (a) and (b) are 1 μm , and that in (c) is 5 μm .

The above results predict that the polymer substrate should swell owing to the presence of the solvent, and the UV-curable acrylate should penetrate into the substrate, while hollow silica nanoparticles cannot penetrate the mixed layer owing to their relative large size during the coating and drying processes (Figure III-9). This prediction applies only to the polymer substrate, because glass substrates were not affected by the solvent and no phase separation occurred. These results demonstrate aggregation hollow silica nanoparticles on the polymer substrate. In addition, these results demonstrate that this aggregation of nanoparticles reduces the reflectance for coating with low-concentration solutions of hollow silica nanoparticles.

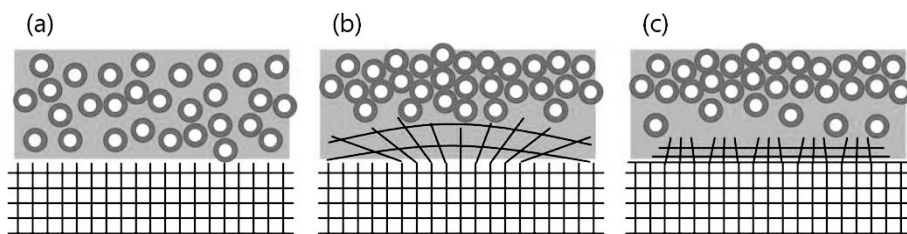


Figure III-9. Aggregation of hollow silica nanoparticles coated on the polymer substrate: (a) immediately after coating, (b) swelling of the substrate induced by the solvent and penetration of the acrylate, (c) the final phase-separated structure.

Commercially available anti-reflection TAC films typically feature a several micrometers thick hard coating layer under the low refractive index layer, for reinforcing the film hardness. For destructive interference, the low refractive index layer should be coated separately with a hard coating layer, which requires at least two coats. Anti-reflective hard coating on TAC substrates can be accomplished in one coating process using solvent swelling-induced surface aggregation of hollow silica nanoparticles. In what follows, a several micrometers thick layer of the HS-AR-30 solution was coated on a TAC film (Figure III-8b), and the optical and mechanical properties of the resulting structure were investigated.

The HS-AR-30 solution, coated on the TAC film, exhibited pencil hardness of H and the minimal reflectance of 2.04% (Figure III-10), which was better than the result of the Takahashi group.^[10]

Coating films with thicknesses on the order of several micrometers can exhibit multiple minimal reflection points in the visible range, which results in the ripple pattern of reflection. However, TAC films coated with HS-AR-30 rarely demonstrated ripple patterns of reflection, implying very weak interference involving reflected light. Based on the distribution of Si in the thickness direction in Figure III-6b, the coating layer of HS-AR-30, coating the TAC film, exhibited a graded distribution of hollow silica nanoparticles, from the upper

surface of the coating layer to the substrate, which induced a gradient refractive index change on the bottom surface of the coating layer.

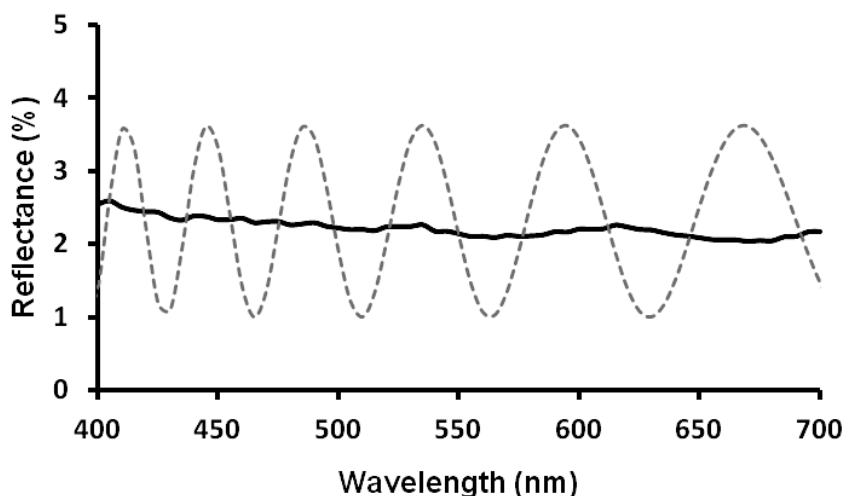


Figure III-10. Reflectance of a TAC film coated with a several micrometers thick layer of HS-AR-30. The black solid line is the measured reflectance, the gray dotted line is the simulated reflectance for the film coated with the 2- μm -thick coating layer with the refractive index of 1.34. The refractive index of the TAC film was 1.47.

As a result, the TAC film coated with the HS-AR-30 solution exhibited only surface reflection, without interface reflection between the coating layer and the substrate. Reflectance for the coating layer with the refractive index of 1.34 was

2.11%, as calculated from Equation I-1, matching well the measured reflectance for the TAC film coated with the HS-AR-30 solution.

Owing to the surface aggregation process in the coating layer that occurred over several micrometers, interface reflection was reduced. This phenomenon is advantageous for fabricating anti-reflection films, because the thickness dependence of destructive interference of light rays can be minimized. Therefore, the need to precisely control the film thickness is also alleviated, increasing the production efficiency of anti-reflection films.

III-4. Conclusions

Coating layers of surface-aggregated hollow silica nanoparticles were prepared on the triacetyl cellulose film. Owing to the solvent swelling of the polymer substrate and penetration of a UV-curable acrylate solution, hollow silica nanoparticles aggregated towards the coating layer's surface. The refractive index of the coating layer containing fully packed hollow silica nanoparticles and acrylate monomers was calculated to be 1.34. Thin coatings with 20 wt% to 60 wt% of silica nanoparticles on the polymer substrate showed the reflectance of about 1.0%. The cross-sectional morphology investigation revealed that surface aggregation of hollow silica nanoparticles occurred on the polymer substrate, but not on the glass substrate. These results suggested that solvent swelling of the polymer substrate was essential for inducing the aggregation of hollow silica nanoparticles. In addition, thick coatings on the polymer substrate yielded the reflectance of 2.0% and pencil hardness of H. This work demonstrates the possibility that anti-reflective hard coatings with thickness-independent optical properties can be obtained in one process.

III-5. References

1. X. Du and J. He, *Chem. Eur. J.*, **2011**, *17*, 8165.
2. S. De, D. Jana, S. K. Medda and G. De, *Ind. Eng. Chem. Res.*, **2013**, *52*, 7737.
3. X. Li and J. He, *ACS Appl. Mater. Interfaces*, 2013, **5**, 5282.
4. Y. Lee, T. Lin, F. Hsu and J. Jan, *Nanoscale*, 2016, **8**, 2367.
5. X. Du and J. He, *Langmuir*, 2011, **27**, 2972.
6. H. Shimomura, Z. Gemici, R. E. Cohen and M. F. Rubner, *ACS Appl. Mater. Interfaces*, 2010, **2**, 813.
7. B. Liu and W. Yeh, *Colloids and Surfaces A: Physicochem. Eng. Aspects*, 2010, **356**, 145.
8. X. Liu and J. He, *J. Phys. Chem. C*, 2009, **113**, 148.
9. A. Wakabayashi, Y. Sasakawa, T. Dobashi and T. Yamamoto, *Langmuir*, 2006, **22**, 9260.
10. T. Shimogaki, H. Tokoro, M. Tabuchi, N. Inoue, T. Tsukamoto, T. Ishii, N. Koike, Y. Yamashina and M. Takahashi, *RSC Adv.*, 2015, **5**, 104792.

Chapter IV.

Anti-reflective and anti-fogging film using mesoporous silica nanoparticles

IV-1. Introduction

Nanoporous structures have been extensively studied for the preparation of anti-reflection films. Because the refractive index of air is nearly 1.0, a coating layer that contains nanopores can reduce the layer's effective refractive index. Several methods of introducing pores into the coating layer have been reported. Stefan Walheim et al. prepared a nanoporous anti-reflection coating by nanophase separation of two polymers, and selective extraction of one polymer by a specific solvent.^[1] Hao Jiang et al. fabricated a porous polymer latex coating by selective dissolution of sacrificial latex particles from a codeposited latex polymer film.^[2,3] Self-assembled structures of block copolymers and polymer-extracted structures from self-assembled morphologies were also investigated.^[4-6] However, it is difficult to scale up these self-assembly processes, and the process of porogen extraction is complex and demanding.

Recently, hydrophobic and hydrophilic surface modifications of anti-reflection films attracted significant attention owing to the potential of these modifications to improve visibility in a variety of situations. The superhydrophilic surface of a film has been obtained using hydrophilic materials with rough surface profiles.^[7-9] Porous silica nanoparticles are good candidate materials for fabricating superhydrophilic anti-reflection films, owing to their low refractive

indices and hydrophilicity. Ling Zhang et al. reported anti-reflection and anti-fogging coatings of loosely packed mesoporous silica nanoparticles, which was fabricated by the layer-by-layer (LbL) deposition method.^[10]

In this study, superhydrophilic anti-reflection films with single-layer structures were prepared using relatively large-size mesoporous silica nanoparticles, and their optical properties were investigated. Morphological changes were induced by controlling the ratio of 150-nm-diameter mesoporous silica nanoparticles to the binder and the morphology effects on the wetting properties were investigated.

IV-2. Experimental

Materials. Hexadecyltrimethylammonium bromide (CTAB) was purchased from TCI. Triethanolamine (TEA) was purchased from Sigma Aldrich. Tetrapropyl orthosilicate (TPOS) was purchased from Sigma Aldrich. N-[tris(3-acrylamidopropoxymethyl)acrylamide was purchased from Wako Chemicals. 1-Hydroxycyclohexyl phenyl ketone was purchased from Sigma Aldrich. Hydrochloric acid (assay above 35%) (HCl) was purchased from Daejung. 1-Butanol was purchased from Junsei Chemicals. Ethanol was purchased from Daejung. Dimethylformamide (DMF) was purchased from Junsei Chemicals. All materials were used as received.

Preparation of silica nanoparticle (S-150). Silica nanoparticles were prepared as described in the literature.^[11] Triethanolamine (0.42 g, 2.82 mmol) and hexadecyltrimethylammonium bromide (CTAB) (2.00 g, 5.49 mmol) were added to 240 mL of water and stirred at 80 °C for 30 min. Tetrapropoxy orthosilicate (TPOS) (3.18 mL, 11 mmol) was added to this solution and stirred vigorously at 80 °C. After stirring for 12 h, the resulting colloidal suspension was filtered using filter paper (Advantec No. 131) and washed several times with ethanol and dried overnight in a vacuum oven.

Preparation of mesoporous silica nanoparticle (MPS-150). Mesoporous silica nanoparticles were prepared by extracting hexadecyltrimethyl ammonium bromide from S-150. 0.5 g of S-150 was added to the mixture of 120 mL of ethanol and 15 mL of HCl and stirred at 60 °C for 24 h. The resulting colloidal suspension was filtered using filter paper (Advantec No. 131) and washed several times with ethanol and dried overnight in the vacuum oven.

Preparation of MPS-150-sol. A colloidal silica dispersion was prepared by dispersing 0.2 g of MPS-150 in 4 g (4.24 mL, 54.72 mmol) of DMF and sonicated for 1 h at room temperature. The total solid content was 4.76 wt%.

Preparation of a UV curable binder solution (B). A UV curable acrylate solution was prepared by dissolving N-[tris(3-acrylamidopropoxymethyl) acrylamide (0.16 g, 0.315 mmol), 1-hydroxycyclohexyl phenyl ketone (0.04 g, 0.20 mmol) in 4 g (4.24 mL, 54.72 mmol) of DMF. The total solid content was 4.76 wt%.

Preparation of a UV curable mesoporous silica coating solution [AF-AR-20~AF-AR-80]. All the coating solutions were prepared simply by mixing the MPS-150 sol and B solution at various ratios. The ratios of the MPS-150 to the

total solid content were 20 wt% (AF-AR-20), 33 wt% (AF-AR-33), 50 wt% (AF-AR-50), 67 wt% (AF-AR-67), and 80 wt% (AF-AR-80). The total solid content of all coating solutions was maintained at 4.76 wt%.

Preparation of superhydrophilic anti-reflection films. Glass substrates were plasma-treated (0.83 kV, 0.94 A) before coating. Series of AF-AR solutions were dropped on plasma-treated glass substrates ($5 \times 5 \text{ cm}^2$), followed by spin-coating at 4000 rpm for 60 s. The coated glasses were UV-cured using a 100 W high-pressure mercury lamp in the presence of gaseous nitrogen. The overall irradiation dose was 400 mJ/cm^2 .

Instrument. Fourier transform infrared (FT-IR) spectra were obtained using an Avatar 360 (Thermo Nicolet) in the ATR mode. TEM images were obtained using a JEOL JEM-2010 microscope at 200 keV. Nitrogen adsorption/desorption measurements, Brunauer–Emmett–Teller (BET) surface areas, and Barrett–Joyner–Halenda (BJH) pore size distributions were obtained and calculated using a Belsorp-Max (BEL Japan, Inc.) apparatus. Reflectance was measured using a K-Mac ST4000-DLX reflectometer. SEM images were obtained using a Hitachi S-4300 FE-SEM. Water contact angles were measured using CAM100 (KSV instruments ltd.). Martens hardness data were obtained

using a Fischer Technology Picodentor HM500.

IV-3. Results and discussion

Mesoporous silica nanoparticles were synthesized as described in the literature.^[11] First, TPOS was hydrolyzed and condensed in the basic condition, which induced formation of colloidal silica nanoparticles with CTAB micelles inside the nanoparticles (S-150). Mesoporous silica nanoparticles (MPS-150) were obtained after extracting CTAB using ethanolic HCl. The extraction of CTAB was confirmed as a reduction in the intensity of the FT-IR absorption characteristic of CTAB, in the 3000–2800 cm^{-1} region (Figure IV-1).

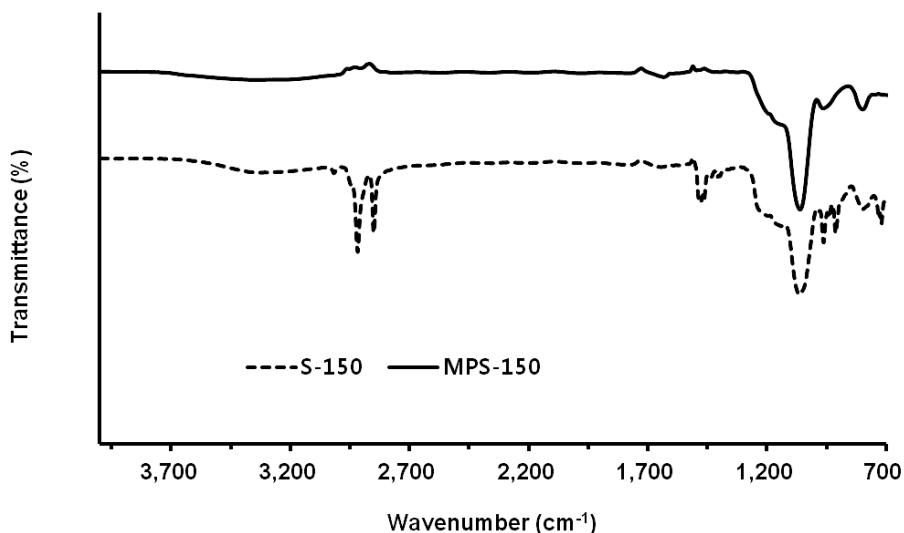


Figure IV-1. FT-IR spectra of S-150 and MPS-150.

The small angle X-ray scattering (SAXS) pattern of MPS-150 exhibited a broad peak with the d -spacing of 49.6 Å (Figure IV-2).

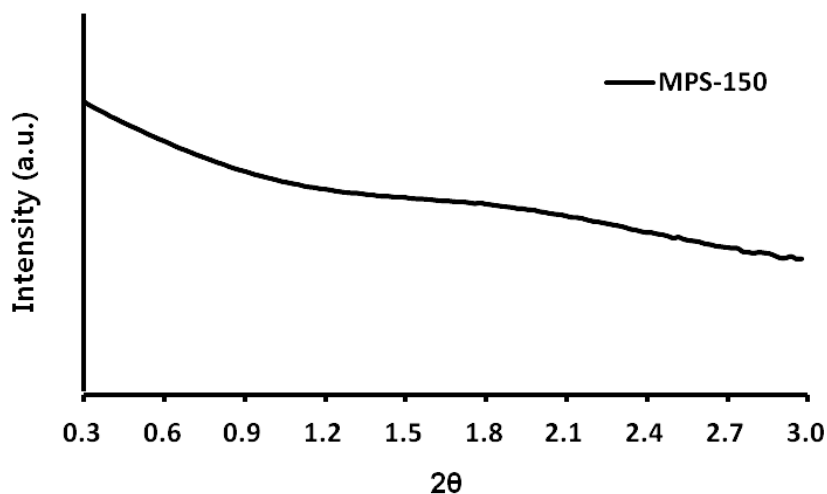


Figure IV-2. SAXS pattern of MPS-150.

Mesoporous silica nanoparticles (Figure IV-3, Figure IV-4) were imaged using SEM and TEM. SEM imaging revealed mesoporous silica with the typical diameter of 150 nm and rough silica surface, owing to the presence of mesopores. TEM imaging revealed dendritic inner pore structures, in a good agreement with previously reported results.^[11]

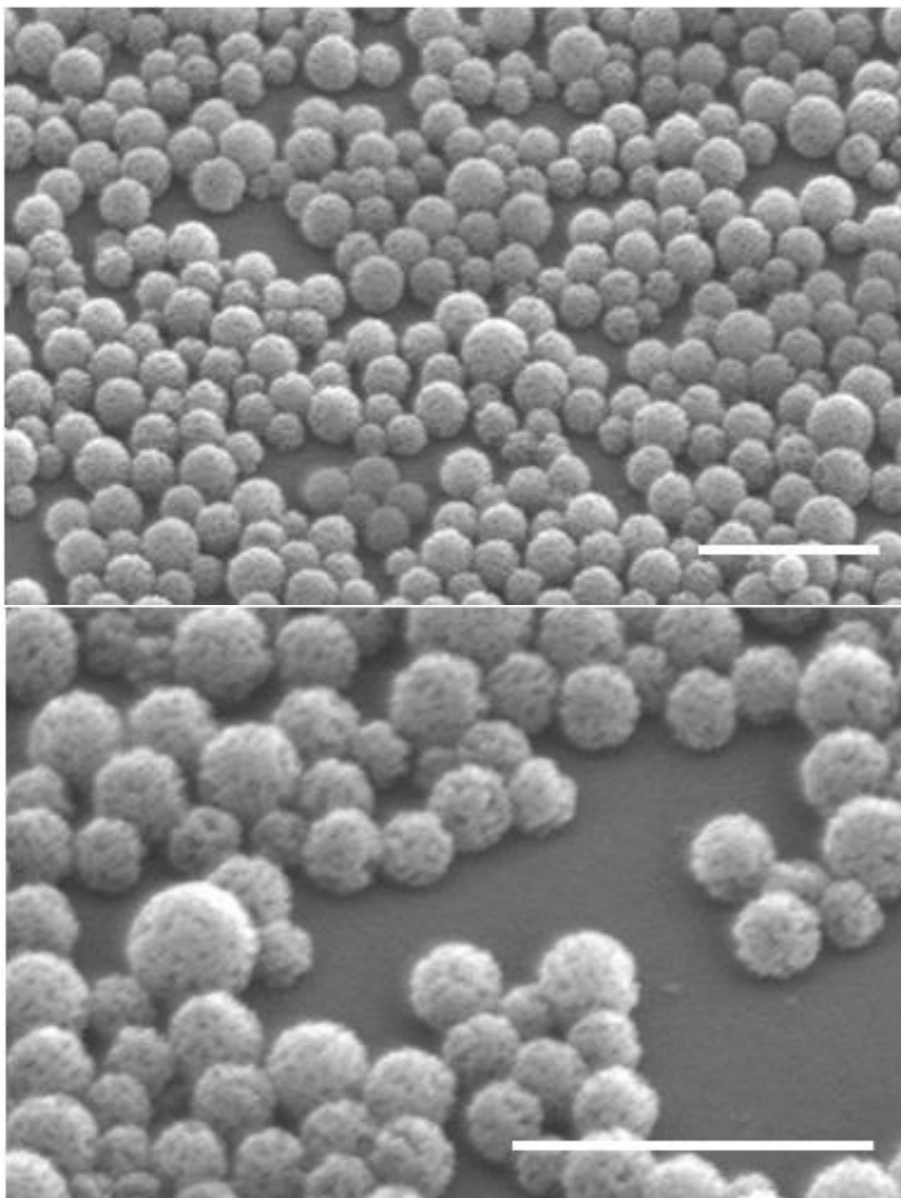


Figure IV-3. SEM images of MPS-150. The scale bar is 500 nm.

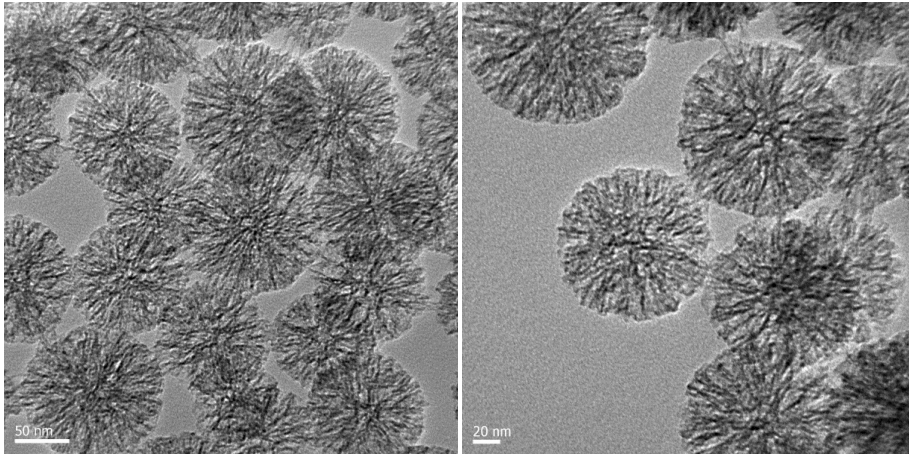


Figure IV-4. TEM images of MPS-150.

Nitrogen adsorption/desorption measurements were performed to investigate the pore structure of MPS-150 (Figure IV-5). The BET surface area of MPS-150 was $787 \text{ m}^2/\text{g}$ and the overall pore volume was $1.52 \text{ cm}^3/\text{g}$. The typical BJH pore size (Figure IV-6), determined from the adsorption branch of the isotherm, was 2.74 nm .

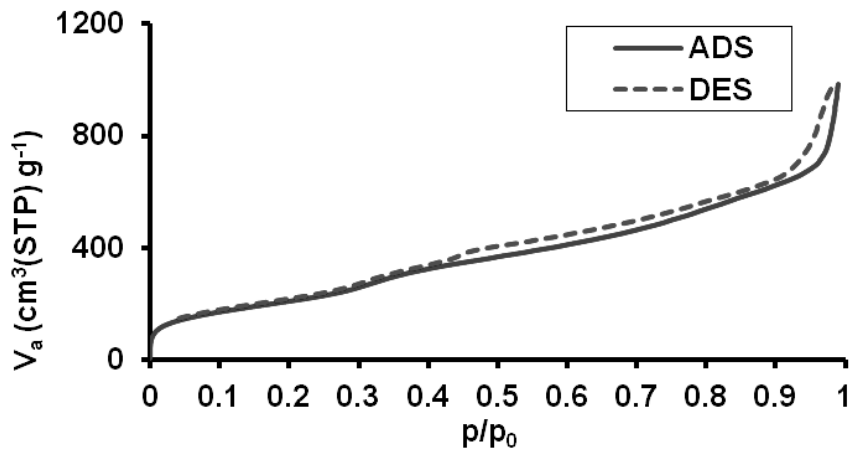


Figure IV-5. Nitrogen adsorption-desorption isotherm for MPS-150.

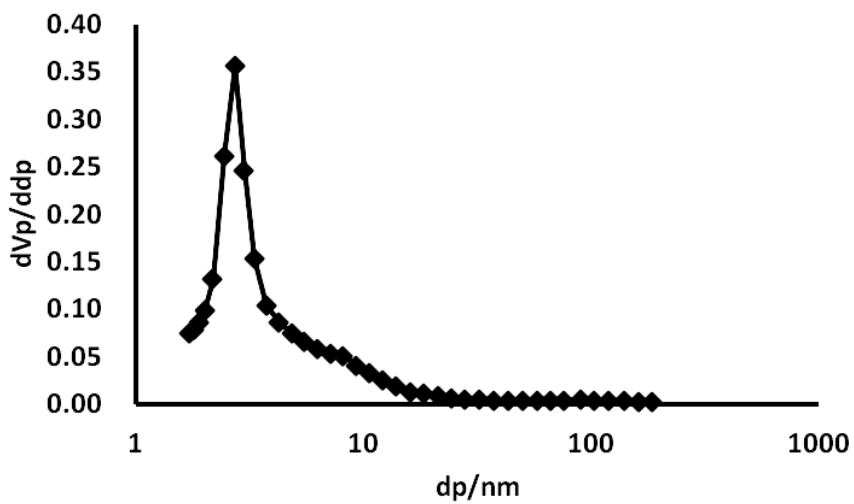


Figure IV-6. BJH pore size distribution for MPS-150.

To prepare superhydrophilic anti-reflection films, nanoporous structures were fabricated. According to Equation I-9 suggested by Wenzel, a superhydrophilic superwetting surface can be accomplished by ensuring a rough surface morphology and hydrophilic materials.^[7] As the roughness factor r increases, the maximal intrinsic contact angle (θ_i) for superwetting increases as well, making it more easier to turn a hydrophilic material into a superhydrophilic one by manipulating its surface roughness. The relation between the angles is

$$\cos \theta_m = r \cos \theta_i \quad (\text{Equation I-9})$$

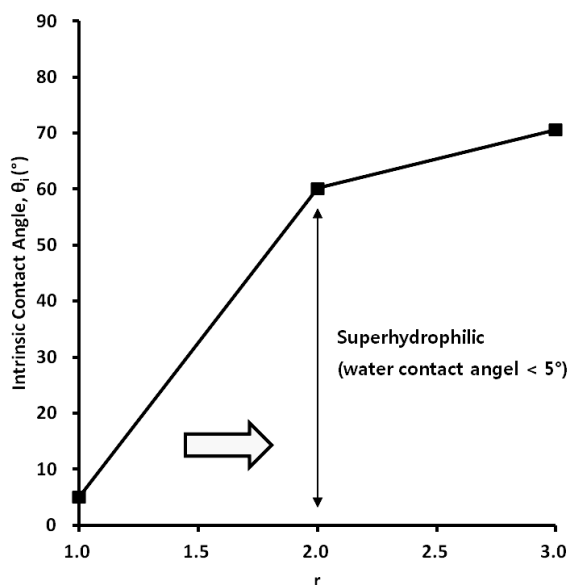


Figure IV-7. Surface roughness factor r vs. the intrinsic contact angle, calculated from the Wenzel equation.

For example, when r is 2, materials with the intrinsic contact angle in the 0° – 60° range are macroscopically superwetting, owing to their surface roughness.

In addition, nanoporous structures can reduce their refractive index, which can induce the anti-reflection property. To achieve these two properties in a single coating process, a single-layer loosely packed structure of 150-nm-diameter mesoporous silica nanoparticles was prepared. The dispersion solvent played a critical role in preparing a uniform single-layer coating of nanoparticles. In this study, water and DMF were considered as dispersion solvents. The coating solution prepared with DMF yielded a well-dispersed single layer of MPS-150, whereas the coating solution prepared with water yielded a coating surface with irregular morphology (Figure IV-8). Low surface tension and high boiling point of DMF, compared with those of water, contributed to the coating surface morphology. The lower surface tension made it easier to wet the substrate, while the higher boiling temperature assured that the deposited nanoparticles had sufficient time to be deposited on the substrate as a single-layer structure.^[12] The single-layer structure of MPS-150 was confirmed by the cross-sectional SEM image (Figure IV-9).

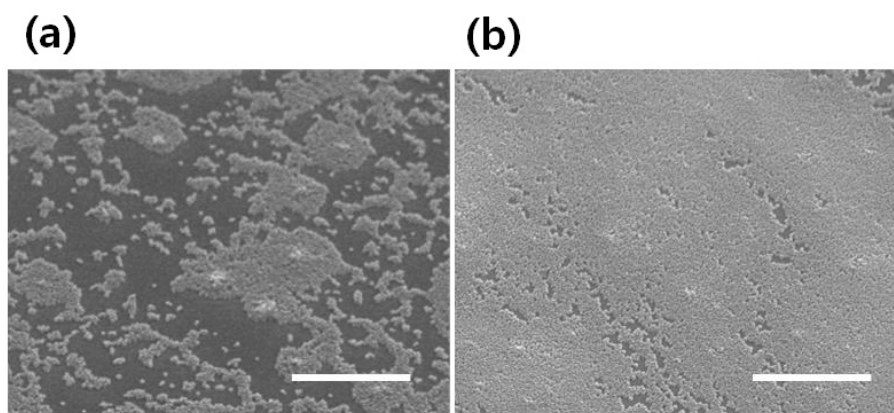


Figure IV-8. SEM images of MPS-150 dispersion in (a) water and (b) DMF.

The scale bar is 5 μm .

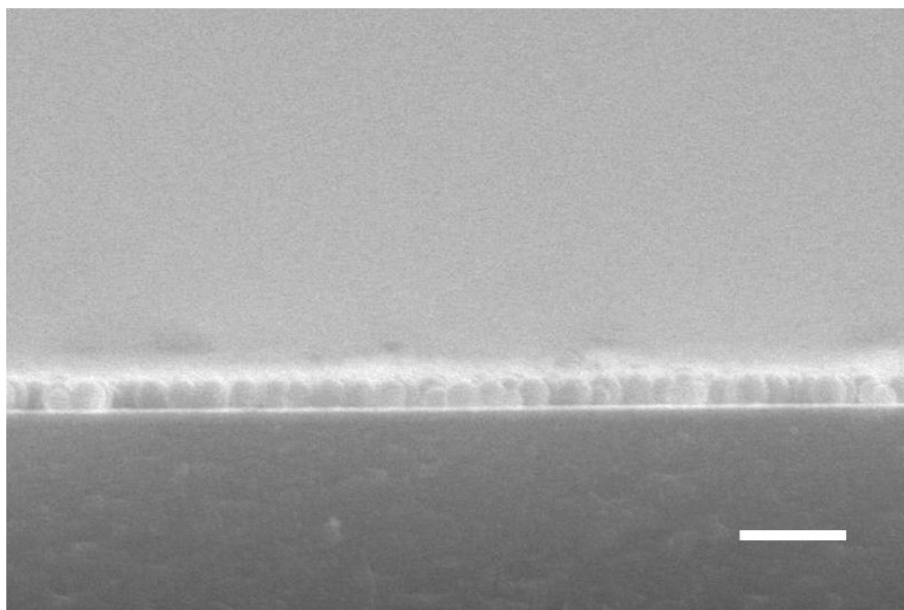


Figure IV-9. Cross-sectional SEM image of MPS-150 dispersion in DMF. The

scale bar is 500 nm.

The synthesized 150-nm-diameter mesoporous silica nanoparticles (MPS-150) were dispersed in DMF and mixed with a UV-curable binder solution at various ratios. Single-layered coatings with MPS-150 were fabricated on plasma-treated glass substrates by spin-coating the prepared solutions at 4000 rpm. The morphologies of the coated surfaces were characterized by SEM measurements (Figure IV-10).

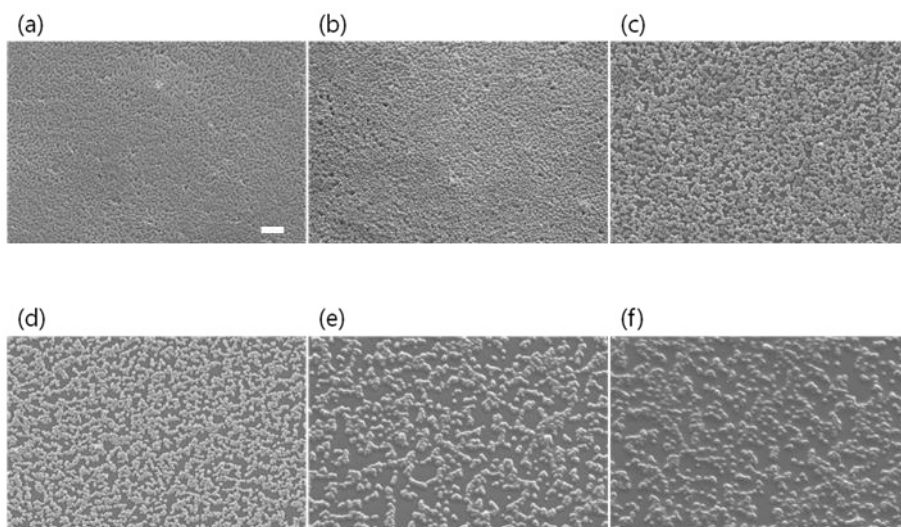


Figure IV-10. SEM images of the coating surfaces with (a) MPS-150 dispersion in DMF, (b) AF-AR-80, (c) AF-AR-67, (d) AF-AR-50, (e) AF-AR-33, and (f) AF-AR-20, respectively. The scale bar is 1 μm and the magnification of all the images is the same.

The dispersion of MPS-150 in DMF without any binder (Figure IV-10. a) yielded a single layer of closely packed silica nanoparticles coating the surface. As the ratio of MPS-150 in the coating solution decreased from 80 wt% (AF-AR-80) to 20 wt% (AF-AR-20), the distance between the MPS-150 particles increased. The increased distance between the nanoparticles was manifested as pores in the single layer and changed the optical properties and wettability of the coating layer. For MPS-150 concentrations in the 100–67 wt% range, increasing the inter-particle space reduced the refractive index of the coating layer, reducing the reflectance from 0.95% to 0.71%. However, from 50 wt% of MPS-150, the reflectance increased and the reflectance for the 20 wt% of MPS-150 exhibited 2.29 % (Figure IV-11).

These results imply that for MPS-150 ratio less than 67 wt%, the inter-particle distance is too large to contribute to reducing the refractive index as a porous structure in the coating layer; rather, for this inter-particle distance the nanoparticle scatter the incident light. This light scattering was parameterized in terms of haze. Haze was defined as the ratio of the transmittance of diffused light to the overall transmittance (Figure IV-12). For MPS-150 layers at 80 wt% and 67 wt% the haze was under 1%, whereas for concentrations under 67 wt% the haze was above 1%, decreasing the optical clarity of the coating layer.

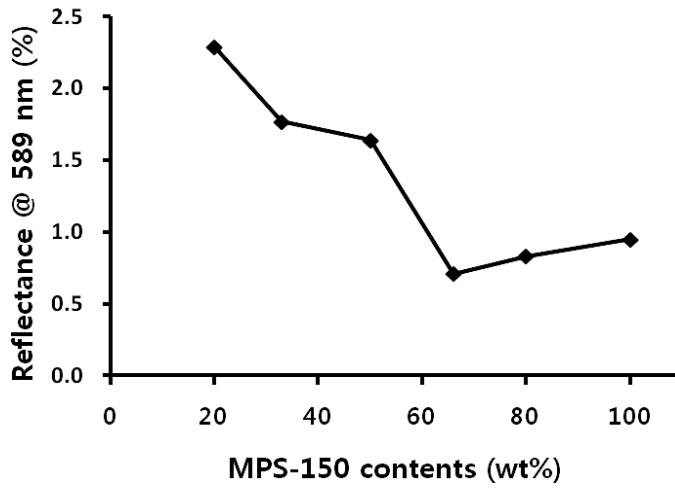


Figure IV-11. Reflectance of the coating film, vs. the MPS-150 ratio.

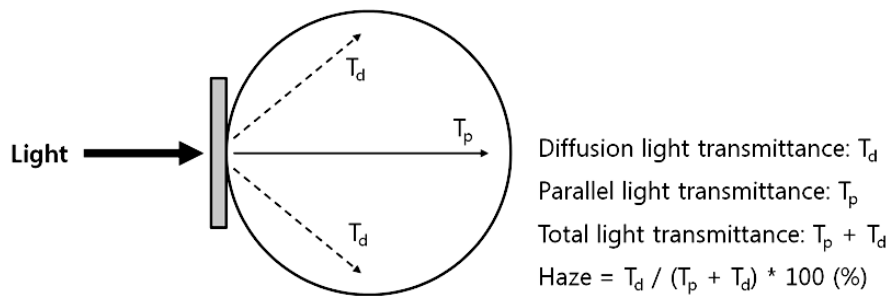


Figure IV-12. Schematic illustration of haze.

Reflection spectrum was measured for light in the visible range (Figure IV-13). The minimal reflectance was 0.71%, obtained at 560 nm. Assuming that the coating layer is a homogeneous single layer, the refractive index of the coating layer was calculated as 1.33 from Equation I-1 and the thickness of the coating

layer was calculated as 105 nm from Equation I-3; note that the calculated thickness is smaller than the diameter of MPS-150. This implies that a fraction of the top surface of a single layer of 150-nm-diameter mesoporous nanoparticles acts as a gradient refractive index layer.

The visibility of anti-reflection films was compared with that of uncoated glass. The uncoated glass film strongly reflected the outside fluorescent lamp light, distorting the image of a letter behind the glass. In the case of anti-reflection coated glass the reflection of the outside light was alleviated, and the letter was clearly visible.

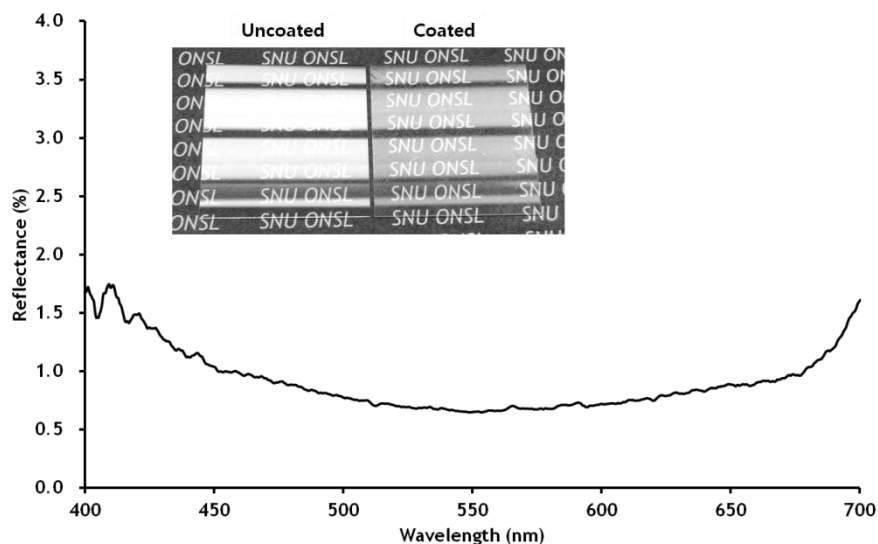


Figure IV-13. Images and reflectance spectrum of the optimal anti-reflection film obtained by coating with solution 2.

Water contact angles of the coating layers were investigated as well (Figure IV-14). For MPS-150 ranging from 100 wt% to 67 wt%, superhydrophilic properties were observed, with the water contact angle under 4°. This was attributed to hydrophilic silica and rough coating surface. However, for MPS-150 concentration below 67 wt%, the water contact angle of the coating increased, reaching the binder layer's water contact angle (56°), implying that the amount of MPS-150 was too small to cover the layer under 67 wt%. Furthermore, as the MPS-150 ratio decreased, the area of the flat surface increased, decreasing the surface roughness factor r . As a result, the macroscopic contact angle increased.

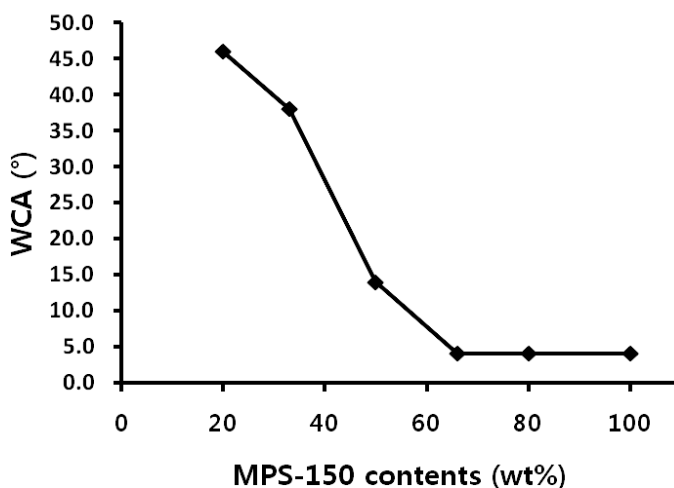


Figure IV-14. Water contact angles of coating films, vs. the MPS-150 concentration.

By virtue of the superhydrophilic properties of the MPS-150 coating layer, the resulting structures exhibited anti-fogging properties (Figure IV-15). To characterize the anti-fogging ability, 67 wt% of MPS-150 coated and uncoated bare glasses were placed in a refrigerator at $-40\text{ }^{\circ}\text{C}$ for 30 min, following which they were kept at room temperature. Because in all cases the coating was applied to one side only, water droplets on the other side of the glasses were wiped out and the visibility of images behind the glasses was investigated.

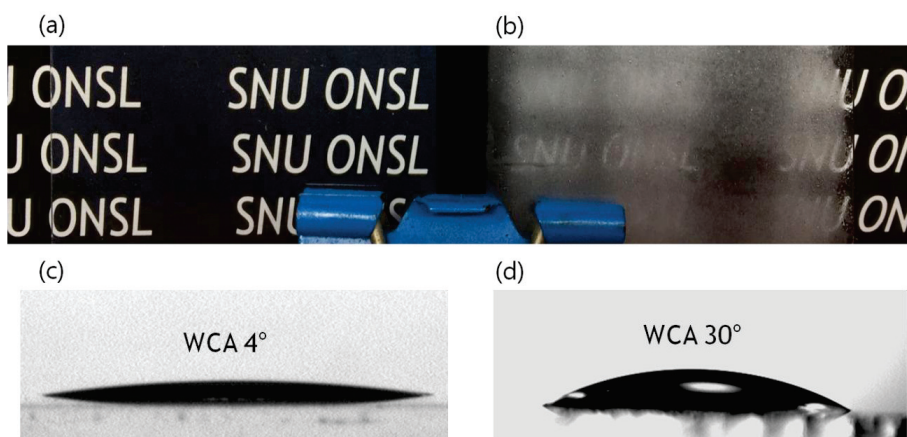


Figure IV-15. Characterization of anti-fogging using images, for a (a) AF-AR-67 coated glass and (b) uncoated glass, and water contact angles for a (c) AF-AR-67 coated glass and (d) uncoated glass.

MPS-150 coated glass exhibited vivid transmission and a sample letter located behind the glass could be clearly read, whereas the surface of the uncoated glass

was fogged, scattering the incident light and blurring the image of the letter located behind the glass.

Finally, the hardness of the coating layer was investigated for different ratios of MPS-150 to the binder (Figure IV-16). As the concentration of MPS-150 decreased (implying an increase in the binder ratio) the Martens hardness increased. The MPS-150 layer at 100 wt% exhibited the lowest hardness of 79 N/m², because there was no binding property to hold the nanoparticles together. The hardness of the MPS-150 layer at 67 wt% was above 100 N/mm² (115 N/mm²), making that coating layer resistant to gentle scratching.

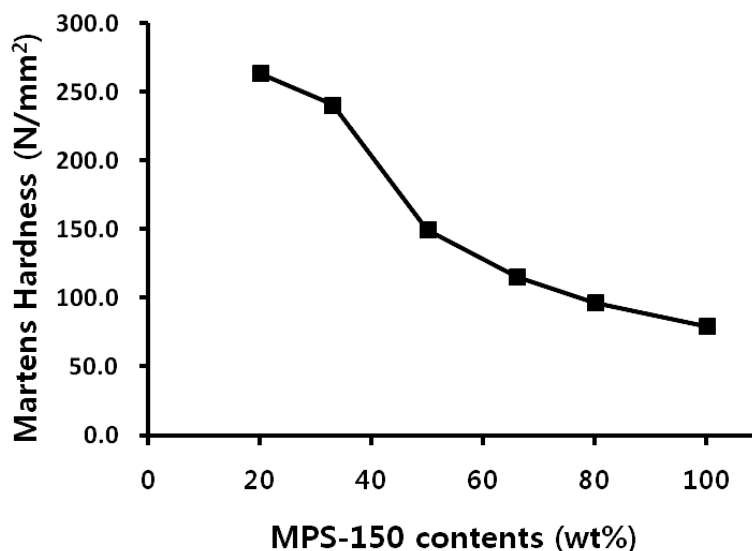


Figure IV-16. Coating film's hardness, vs. the MPS-150 concentration.

IV-4. Conclusions

Mesoporous silica nanoparticles with a diameter of 150 nm (MPS-150) were synthesized and used for a single-layer superhydrophilic anti-reflection film coating. By controlling the ratio of MPS-150 to the binder, porous anti-reflection films were obtained without employing any other porogens or extraction processes. It was observed that the inter-particle distance effectively reduced the refractive index and reflectance in the coatings with MPS-150 of up to 67 wt%. The coatings also demonstrated anti-fogging properties, which was attributed to superhydrophilic surfaces resulting from hydrophilic silica and rough surfaces formed by them.

IV-5. References

1. S. Walheim, E. Schäffer, J. Mlynek and U. Steiner, *SCIENCE*, 1999, **283**, 520.
2. H. Jiang, W. Zhao, C. Li and Y. Wang, *Polymer*, 2011, **52**, 778.
3. H. Jiang, W. Zhao, C. Li and Y. Wang, *Soft Matter*, 2011, **7**, 2817.
4. W. Joo, M. S. Park and J. K. Kim, *Langmuir*, 2006, **22**, 7960.
5. W. Joo, H. J. Kim and J. K. Kim, *Langmuir*, 2010, **26**, 5110.
6. X. Li and Y. Han, *J. Mater. Chem. C*, 2013, **1**, 2266.
7. R. N. Wenzel, *Ind. Eng. Chem.*, 1936, **28**, 988.
8. A. B. D. Cassie and S. Baxter, *Trans. Faraday Soc.*, 1944, **40**, 546.
9. J. Drelich and E. Chibowski, *Langmuir*, 2010, **26**, 18621.
10. L. Zhang, Z. Qiao, M. Zheng, Q. Huo and J. Sun, *J. Mater. Chem.*, 2010, **20**, 6125.
11. H. Yamada, C. Urata, H. Ujiie, Y. Yamauchi and Kazuyuki Kuroda, *Nanoscale*, 2013, **5**, 6145.
12. J. Choi, T. L. Alford and C. B. Honsberg, *Langmuir*, 2014, **30**, 5732.

국문요약

반사방지는 반사된 빛의 상쇄 간섭을 이용하여 물질 표면에서 반사되는 빛을 제거하는 기술이다. 반사방지 층으로 저굴절률을 가지는 실리카 나노입자층이 다양하게 연구되고 있다. 저굴절 특성은 메조포러스 실리카나 중공 실리카 자체의 기공에 의해 달성할 수 있을 뿐 아니라 나노입자의 적층 시 발생하는 입자 간의 기공 구조에 의해서도 달성할 수 있다. 다양한 환경에서 반사방지 필름의 성능을 향상시키기 위해 광 감응성 특성이나 초친수 특성에 기인한 김서림 방지 등과 같은 부가적인 기능 또한 연구되고 있다.

본 연구에서는, 실리카 나노입자를 가진 반사방지 필름을 제조하고 그들의 특성과 응용에 대해 조사하였다.

첫째, 고굴절층으로 광루미네선스 유로피움(III) 복합체를 함유한 자외선 경화형 아크릴레이트와, 저굴절층으로 콜로이달 나노실리카층을 가지는 감광성 2 층 구조 반사방지 필름을 제조하였다. 고굴절층의 굴절률은 유로피움(III) 복합체의 함량이 증가함에 따라 1.53 에서 1.69 까지 조절할 수 있었다. 글래스 상에서 반사방지 필름의 반사율은 두 층의 굴절률과 두께를 조절하여 0.48 %까지 저감할 수 있었다. 이 반사방지 필름을 LCD 상에 부착한 후 광학적 특성을 조사하였다. 유로피움(III) 복합체의 흡수와 여기 파장이 LCD 백라이트의 파장과 거의 겹치지 않기 때문에 반사방지층에 있는 유로피움(III) 복합체는 디스플레이의 화면 영상을 왜곡하지 않았다. 디스플레이 이미지는 반사방지 특성에 의해 실내의 형광등 아래에서도 잘 볼 수 있었다. 또한 레이저 빛을 이용하여 디스플레이 스크린의 특정 부위를 표시하는 것이 가능하였다. 405 nm 레이저

포인터가 특정 영역을 비추면, 그 영역이 유로피움(III) 복합체의 발광에 의해 밝은 붉은 점으로 나타났다.

두 번째로, 중공 실리카 입자의 표면 집적화를 통해 고분자 기재 상에 반사방지 필름을 제조하였다. 10 nm 두께의 벽을 가진 80 nm 크기의 중공 실리카 입자는 1.27의 굴절률을 보였다. 용제에 의한 고분자 기재의 팽창과 자외선 경화형 아크릴레이트의 기재 침투로, 저굴절률을 가지는 중공 실리카가 코팅층 표면에 집적화되어 반사방지층을 형성하였고, 이 층의 굴절률은 1.34였다. 고분자 필름 상에 20 wt% ~ 60 wt%의 중공 실리카 분산액을 코팅하여 반사율 약 1% 이하의 반사방지층을 제조할 수 있었다. 또한, 수 마이크로미터 두께의 코팅을 실시하여, TAC 기재 상에서 연필경도 H의 반사방지 하드코팅 필름을 제조하였다. 수 마이크로미터 두께의 반사방지 하드코팅 필름은 중공 실리카의 상분리 현상에 의해 코팅 내부의

연속적인 굴절률층이 형성되어, 코팅층과 기재 사이의 계면 반사를 억제하였고, 필름 표면만의 반사로, 반사율 2%의 필름을 형성하였다.

세 번째로, 150 nm 크기의 메조포러스 실리카 나노입자의 단일층 형성을 통한 초친수 반사방지 필름을 제조하였다. 메조포러스 실리카와 바인더의 혼합비를 조절함으로써, 간단히 코팅층의 표면 형상을 제어할 수 있었으며, 제조한 필름은 실리카의 화학적 친수성과 실리카 단일층의 표면 거칠기로 인해 반사방지 기능과 김서림 방지 기능을 동시에 보였다. 67 중량 퍼센트의 메조포러스 실리카 코팅에서, 0.71%의 가장 낮은 반사율을 보였다. 초친수 성능으로 인해, 67 중량 퍼센트의 메조포러스 실리카 층이 코팅된 글래스는 김서림 테스트 시 즉시 투과 선명성을 회복하였다.

주요어: 반사방지, 광루미네선스, 메조포러스, 실리카, 저굴절률, 초친

수성, 김 서림 방지, 표면 집적화

학번: 2009-30155